SUPPORTING INFORMATION

A Dysprosium Single Molecule Magnet outperforming current pseudocontact shift agents

Francielli S. Santana[a] †, Mauro Perfetti[b,c] †, Matteo Briganti[a,b], Francesca Sacco[b,d,e], Giordano Poneti[f], Enrico Ravera[b,d,e]*, Jaisa F. Soares[a]*, Roberta Sessoli[b,c]*

[a] Departamento de Química, Universidade Federal do Paraná, Centro Politécnico, 81530-900 Curitiba, PR, Brazil.

[b] Department of Chemistry "U. Schiff", University of Florence, Via della Lastruccia 3-13, 50019, Sesto Fiorentino (FI), Italy.

[c] Research Unit Firenze, INSTM, I-50019 Sesto Fiorentino, Firenze, Italy,

[d] Magnetic Resonance Center, University of Florence, Via Luigi Sacconi 6, 50019, Sesto Fiorentino (FI), Italy

[e] Consorzio Interuniversitario Risonanze Magnetiche di Metalloproteine, Via Luigi Sacconi 6, 50019, Sesto Fiorentino (FI), Italy

[f] Instituto de Química, Universidade Federal do Rio de Janeiro, Avenida Athos da Silveira Ramos, 149, Centro de Tecnologia – Cidade Universitária, 21941-909 Rio de Janeiro, Brazil

† These authors contributed equally.

Synthesis and general characterization

All commercial reagents were purchased from Sigma-Aldrich and used as received. Methanol was dried and distilled by standard procedures.[1] The proligand *N*,*N*'-bis(2-hydroxybenzyl)-*N*,*N*'-bis(2-methylpyridyl)-1,2-propanediamine (H_2bbppn) was prepared according to the literature[2, 3] and characterized by several analytical techniques as previously described by some of us.[4] Carbon, hydrogen, nitrogen and metal contents were determined by MEDAC Laboratories Ltd. (Chobham, Surrey, UK). Mid-infrared (FTIR, 400-4000 cm^{-1}) spectra were registered from KBr pellets on Bruker Vertex 70 equipment with a resolution of 4 cm^{-1}. Powder X-ray diffraction analysis (Cu-Kα, λ = 1.5406 Å) was carried out at 40 kV and 30 mA, with sampling pitch and a scan speed of 0.02° and 1° min^{-1}, respectively, on a Shimadzu-600 diffractometer. The 2θ range of 5 - 55° was employed in the measurements. The calculated powder diffraction pattern (PXRD, Figure S5) of **1** was generated from the single-crystal crystallographic information file (CIF) using the Mercury 4.0 software.[5]

Synthesis of complex 1, [Dy(bbppn)Cl]

To a solution of 0.145 g (0.387 mmol) of $DyCl_3 \cdot 6H_2O$ and 0.181 g (0.387 mmol) of H_2bbppn in 20 mL of methanol, 108 µL of triethylamine (78.4 mg, 0.775 mmol) were added with stirring. This produced a white suspension that was stirred at 50 °C for 2 h under N_2 and then filtered in air at room temperature. The resulting colourless solution was submitted to vapor diffusion with diethyl ether (MeOH:Et_2O 1:1). The remaining solid (0.068 g) was then stirred for 12 h in 50 mL of CH_2Cl_2 to give a fine suspension, which was also filtered and submitted to vapor diffusion with Et_2O (CH_2Cl_2:Et_2O 1:1). After 3-7 days at room temperature, colourless rhombs were isolated by filtration from both mixtures, washed with cold methanol and acetone, and dried under vacuum. Total yield: 0.107 g (42 %). Complex **1** is soluble in dimethyl sulfoxide, slightly soluble with heating in dichloromethane and methanol, and insoluble in hexane, toluene, tetrahydrofuran, dimethoxyethane, chloroform, and dimethylformamide. Anal. Found: C, 52.60; H, 4.36; N, 8.32. Calcd for $C_{29}H_{30}ClDyN_4O_2$: C, 52.41; H, 4.55; N, 8.43.

Synthesis of complex 4, [Y(bbppn)Cl]

Complex **4** was prepared by a procedure analogous to that employed for **1**. Quantities were 0.178 g (0.587 mmol) of $YCl_3 \cdot 6H_2O$, 0.275 g (0.587 mmol) of H_2bbppn, and 164 µL (119 mg, 1.18 mmol) of triethylamine in 30 mL of methanol. From the vapor diffusion mixtures, colorless rhombs were isolated after 4-5 days. Total yield: 0.209 g (49 %). The solubility profile of complex **4** is very similar to that of **1**. Anal. Found: C, 58.53; H, 5.07; N, 9.34. Calcd for $C_{29}H_{30}ClN_4O_2Y$: C, 58.94; H, 5.12; N, 9.48.

Synthesis of the solid solution of [Dy(bbppn)Cl]@[Y(bbppn)Cl], 1[Y]

The **1[Y]** crystalline solution was obtained by combining 10.0 mg (0.0265 mmol) of $DyCl_3 \cdot 6H_2O$ and 0.154 g (0.507 mmol) of $YCl_3 \cdot 6H_2O$ (*ca* 1:19 molar ratio) with 0.250 g (0.534 mmol) of H_2bbppn and 149 µL (108 mg, 1.07 mmol) of triethylamine. The experimental procedure was analogous to that employed for the preparation of **1**. Total yield: 0.241 g (81 %). The solubility profile of **1[Y]** is very close to those of **1** and **4**. Anal. Found: C, 58.25; H, 5.10; N, 9.32; Dy, 1.79; Y, 13.46. These results correspond to the formulation $C_{29.16}H_{30.37}N_{4.00}Dy_{0.07}Y_{0.91}$ (oxygen and chlorine not measured), or a Dy : Y proportion of 7 : 93 mol%.

Single-crystal X-ray diffraction analysis

Diffraction intensities were collected on a Bruker D8 Venture diffractometer equipped with a Photon 100 CMOS detector, Mo-K_α radiation (λ = 0.71073 Å), and graphite monochromator. Colorless crystals of **1** and **4** were mounted on MiTeGen microloops, and intensity data were measured at room temperature by thin-slice ω-and φ-scans. Data were processed using the APEX3 program. The structures were solved by intrinsic phasing methods in SHELXT,[6, 7] and all non-hydrogen atoms were refined anisotropically by full-matrix least-squares on F^2 using the SHELXL program suite.[7] Anisotropic thermal parameters were assigned to all non-hydrogen atoms. Scattering factors for neutral atoms were taken from the International tables for X-ray crystallography. All hydrogen atoms were included in idealized positions with U(iso)'s set at 1.2U(eq) or, for the methyl group hydrogen atoms, 1.5U(eq) of the parent carbon atoms. All computer programs were run through WinGX,[8] and the diagrams were drawn with the Diamond software.[9] Data for **1** and **4** have been deposited at the Cambridge Structural Database with the following CCDC numbers: CCDC-2129444 for [Dy(bbppn)Cl] (**1**) and CCDC-2129445 for [Y(bbppn)Cl] (**4**).

In the structures of **1** and **4**, C15 (in the ethylenediamine bridge) is disordered over two positions about C14A and C14A^i (Figures 1 and S1); in the refinement, the occupancy ratio was fixed at 50/50. This disorder is a consequence of a crystallographic 2-fold rotation axis that bisects the C14A−C14A^i bond and coincides with the Ln−Cl bond direction. Because of this disorder involving the methyl group, the two carbon atoms of the ethylenediamine moiety had to be considered both as methine and methylene groups depending on the position of the disordered C15. Consequently, arriving at the best refinement model required the addition of C14A (bound to C15) and symmetry-generated C14A^i, together with C14B and symmetry-generated C14B^i (without C15; neither shown in Figures 1 and S1), which are methylene carbon atoms. To all these atoms (C14A, C14A^i, C14B, C14B^i, and all hydrogen atoms attached), an occupancy factor of 0.5 was assigned to generate the correct atom counting for the complete structure.

Table S1. Crystal data and structure refinement for complexes **1** and **4**

Elemental formula	**$C_{29}H_{30}ClDyN_4O_2$ (1)**	**$C_{29}H_{30}ClN_4O_2Y$ (4)**
CCDC deposition number	2129444	2129445
Molar mass / g mol^{-1}	664.52	590.93
Crystal system, space group	Monoclinic, *C*2/c	Monoclinic, *C*2/c
Temperature data collection / K	296(2)	300(2)
Wavelength / Å	0.71073	0.71073
a / Å	17.6920(8)	17.7054(7)
b / Å	10.2893(5)	10.2696(4)
c / Å	15.0931(6)	15.0884(6)
α / °	90	90
β / °	103.871(2)	104.0230(10)
γ / °	90	90
V / Å^3	2667.4(2)	2661.72(18)
Z	4	4
ρ_{calc} / Mg m^{-3}	1.655	1.475
μ / mm^{-1}	2.935	2.325
F(000)	1324	1216
Crystal color and shape	Colorless rhomb	Colorless rhomb
Crystal size / mm	0.152 x 0.131 x 0.061	0.227 x 0.108 x 0.106
θ range / °	27.5	26.0
Completeness to θ = 25.2 ° / %	99.8	99.7
Reflections collected	66286	35862
Unique data	3062 (R_{int} = 0.051)	2615 (R_{int} = 0.056)
Observed data	2866	2353
Data / restraints / parameters	3062 / 0 / 174	2615 / 0 /174
Goodness-of-fit on F^2	1.126	1.046
R_1, [I > 2σ(I)], wR_2, [I > 2σ(I)][(*)7]	0.029, 0.070	0.031, 0.071
R_1, wR_2, (all data)	0.033, 0.071	0.037, 0.073
Largest diff. peak and hole / e Å^{-3}	1.11 and –1.40	0.52 and –0.41

(*) **(1)** $w = [\sigma^2(Fo^2)+(0.0283*P)^2+12.1752*P]^{-1}$ with $P = (Fo^2+2Fc^2)/3$
(4) $w = [\sigma^2(Fo^2)+(0.0332*P)^2+3.7418*P]^{-1}$ with $P = (Fo^2+2Fc^2)/3$

Table S2. Selected bond lengths (Å) and angles (°) for complexes **1** and **4**, with estimated standard deviations in parentheses

Bond lengths			
1		**4**	
Dy–O1	2.161(3)	Y–O1	2.1650(16)
Dy–O1^{i}	2.161(3)	Y–O1^{i}	2.1650(16)
Dy–N1	2.545(3)	Y–N1	2.541(2)
Dy–N1^{i}	2.545(3)	Y–N1^{i}	2.541(2)
Dy–N2	2.583(3)	Y–N2	2.5818(19)
Dy–N2^{i}	2.583(3)	Y–N2^{i}	2.582(2)
Dy–Cl	2.5910(16)	Y–Cl	2.5837(9)
C14a–C14a^{i}	1.493(10)	C14a–C14a^{i}	1.526(6)
C14a–C15	1.599(10)	C14a–C15	1.570(6)
Bond angles			
1		**4**	
O1–Dy–O1^{i}	167.19(15)	O1–Y–O1^{i}	168.00(9)
O1–Dy–N1	101.63(11)	O1–Y–N1	102.07(7)
O1^{i}–Dy–N1	79.67(11)	O1^{i}–Y–N1	79.19(7)
O1–Dy–N1^{i}	79.67(11)	O1–Y–N1^{i}	79.19(7)
O1^{i}–Dy–N1^{i}	101.63(11)	O1^{i}–Y–N1^{i}	102.06(7)
N1–Dy–N1^{i}	168.55(17)	N1–Y–N1^{i}	168.17(10)
O1–Dy–N2	73.92(11)	O1–Y–N2	74.28(6)
O1^{i}–Dy–N2	95.39(11)	O1^{i}–Y–N2	95.69(7)
N1–Dy–N2	65.81(11)	N1–Y–N2	66.22(6)
N1^{i}–Dy–N2	125.00(11)	N1^{i}–Y–N2	124.93(7)
O1–Dy–N2^{i}	95.39(11)	O1–Y–N2^{i}	95.69(7)
O1^{i}–Dy–N2^{i}	73.92(11)	O1^{i}–Y–N2^{i}	74.28(6)
N1–Dy–N2^{i}	125.00(11)	N1–Y–N2^{i}	124.93(7)
N1^{i}–Dy–N2^{i}	65.81(11)	N1^{i}–Y–N2^{i}	66.22(6)
N2–Dy–N2^{i}	69.71(15)	N2–Y–N2^{i}	69.50(9)
O1–Dy–Cl	96.41(8)	O1–Y–Cl	96.00(5)
O1^{i}–Dy–Cl	96.40(8)	O1^{i}–Y–Cl	96.00(5)
N1–Dy–Cl	84.27(8)	N1–Y–Cl	84.08(5)
N1^{i}–Dy–Cl	84.27(8)	N1^{i}–Y–Cl	84.08(5)
N2–Dy–Cl	145.14(8)	N2–Y–Cl	145.25(5)
N2^{i}–Dy–Cl	145.14(8)	N2^{i}–Y–Cl	145.25(5)
N2–C14a–C15	108.1(5)	N2–C14a–C15	108.9(3)

Symmetry codes: (i) –x+1, y, –z+3/2; (ii) –x, y, –z+1/2

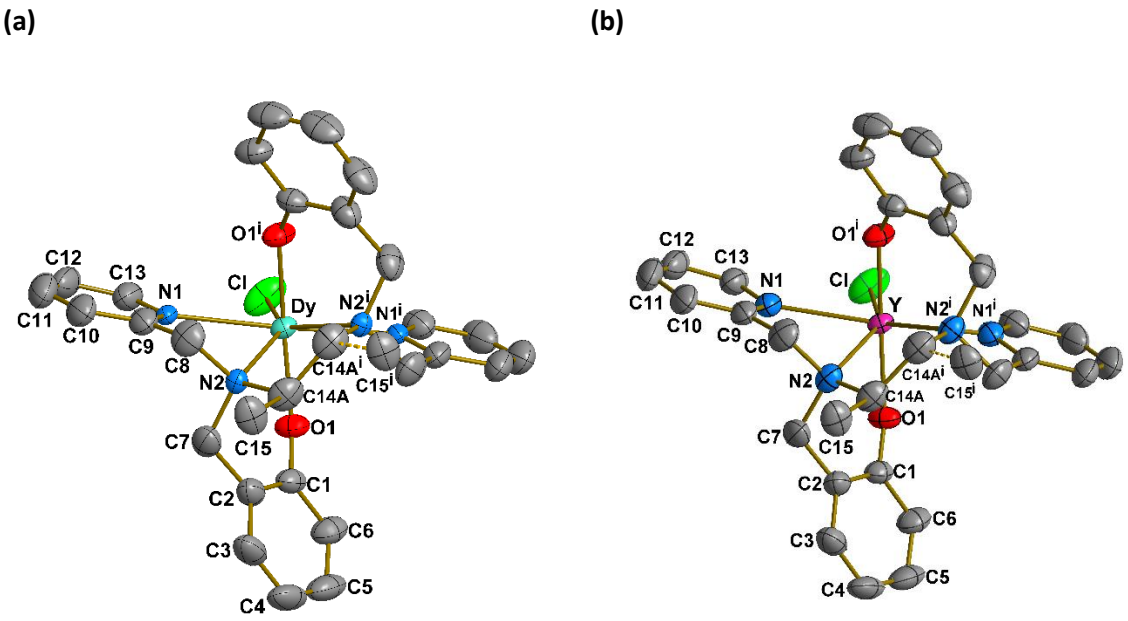

Figure S1. Ellipsoid-type view of complexes **(a)** [Dy(bbppn)Cl] (**1**) and **(b)** [Y(bbppn)Cl] (**4**) indicating the atom numbering scheme. The bond to the disordered carbon C15^{i} is represented by a dashed line. The thermal ellipsoids are drawn at the 50% probability level. Hydrogen atoms were omitted for clarity. Symmetry code (i): 1 -x+1,y,-z+3/2.

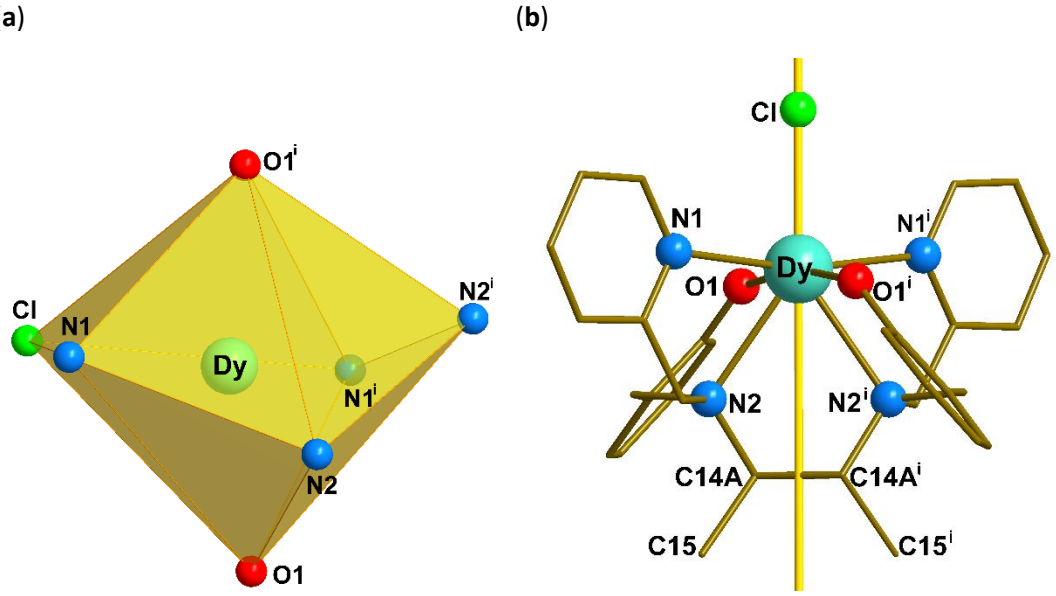

Figure S2. (**a**) Representation of the coordination environment of the Dy^{3+} ion; (**b**) Representation of complex **1** showing the crystallographic 2-fold axis (yellow line), which passes along the Dy–Cl bond and bisects the C14A–C14A^{i} bond.

Table S3. Continuous shape measures of coordination polyhedra for complexes [Dy(bbppn)Cl], **1**, [Dy(bbpen)Cl],[10] **2**, and [Dy(bbpen-CH_3)Cl],[11] **3**, obtained by the use of the SHAPE 2.1 software[12]

Geometry	1	2	3
Heptagon (D_{7h})	34.656	33.833	33.230
Hexagonal pyramid (C_{6v})	21.922	22.436	23.340
Pentagonal bypiramid (D_{5h})	**3.530**	**2.048**	**1.824**
Capped octahedron (C_{3v})	4.820	8.482	7.899
Capped trigonal prism (C_{2v})	3.928	6.898	6.102
Johnson pentagonal bypiramid J13 (D_{5h})	4.533	2.351	2.209
Johnson elongated triangular pyramid J7 (C_{3v})	20.529	20.701	21.882

Table S4. Comparison of selected geometric parameters for complexes [Dy(bbppn)Cl], **1**, [Dy(bbppen)Cl], **2**, and [Dy(bbpen-CH_3)Cl], **3**

Compound	$\Delta L_{equat\ (max)}$ / Å [(a)]	$\Delta D_{plane\ (max)}$ / Å [(b)]	ΔB_{axial} / ° [(c)]	Dy–O_{axial} / Å	Reference
1	0.046	0.579	12.8	2.161(3)	this work
2	0.102	0.224	25.7	2.166(4)	[10]
3	0.089	0.221	21.9	2.155(3), 2.161(3)	[11]

[(a)] $\Delta L_{equat\ (max)}$: difference between the smallest and the largest bond lengths in the equatorial plane.
[(b)] $\Delta D_{plane\ (max)}$: maximum distance between the donor atoms and the average equatorial plane.
[(c)] ΔB_{axial}: maximum O–Dy–O bond angle deviation from linearity.

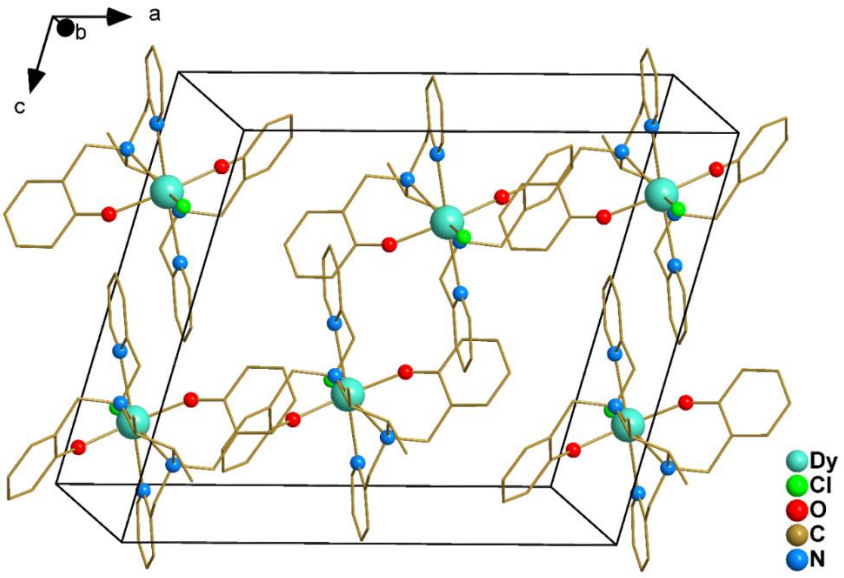

Figure S3. Packing of complex **1** nearly down the *b*-axis. Hydrogen atoms were omitted for clarity.

Table S5. Distances (Å) between Dy^{3+} ions in neighboring molecules of complexes **1** and **4** along the *a*, *b* and *c* directions

Direction	Complex **1**	Complex **4**
along *a*	10.2332(4)	10.2341(4)
along *b*	10.2893(6)	10.2696(6)
along *c*	8.6879(3)	8.6972(3)

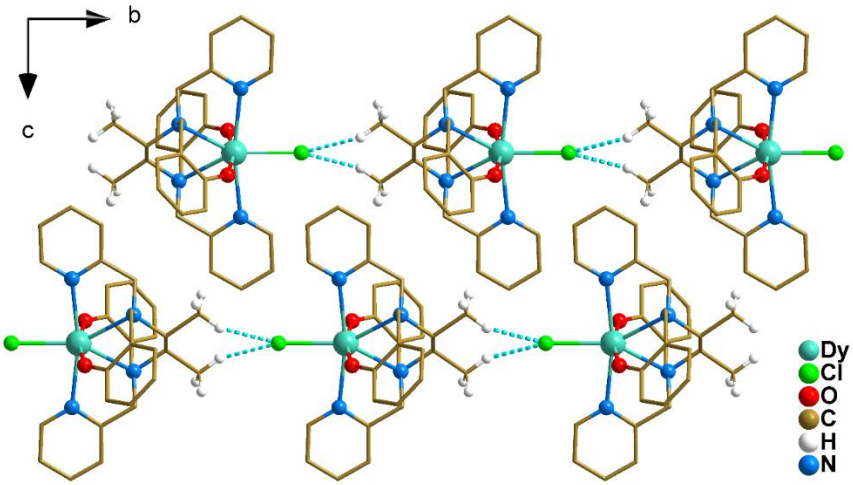

Figure S4. Representation of the intermolecular contacts (light-blue dashed lines) in the crystal structure of **1** ($H15\cdots Cl^{iii}$: 2.58 Å; $C15–H15\cdots Cl^{iii}$: 149.8 °) viewed on the *bc* plane. Symmetry code (iii): x,y+1,z.

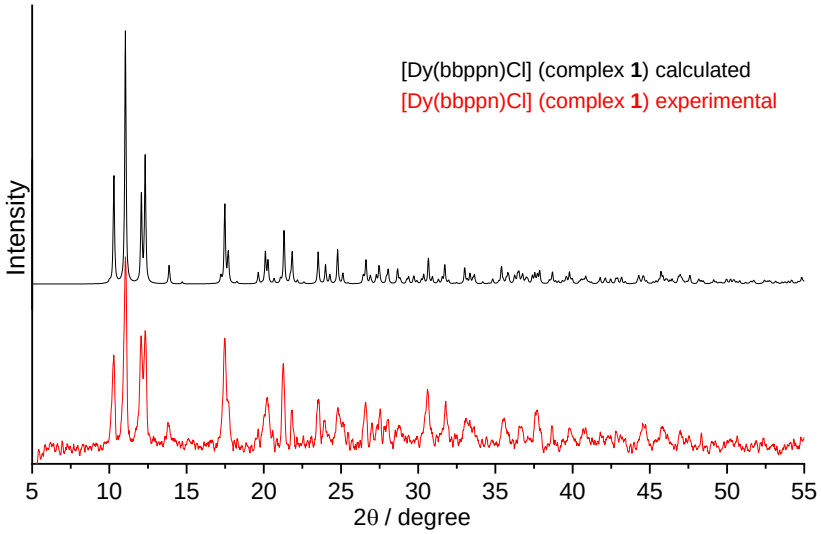

Figure S5. Experimental and simulated PXRD patterns obtained for complex **1**.

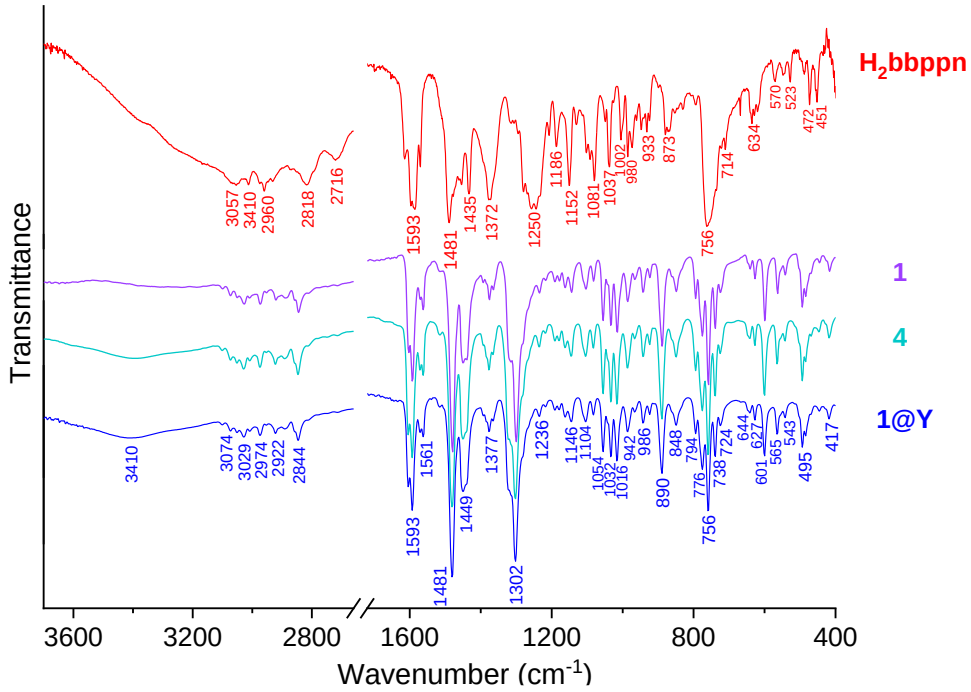

Figure S6. FTIR spectra for **1**, **4**, **1[Y]**, and the proligand **H_2bbppn** (KBr pellets).

The vibrational spectra of **H_2bbppn** and the products **1**, **4**, and **1[Y]** are characterized by the partial overlapping of absorptions from the diamine and the aromatic phenol(ate) and pyridine rings, which spread over the whole spectral range (Table S6). The deprotonation of **H_2bbppn** is confirmed by the absence of the broad band at 3600-2600 cm^{-1}, which is attributed to the symmetric and asymmetric stretchings of the O—H bond, and of the intense O—H bending absorption at 1372 cm^{-1}. Additionally, this deprotonation strongly influences the ν(C—O) band energy, leading to a shift from 1250 cm^{-1} in the proligand to 1302 cm^{-1} in the complexes. Table S6 contains additional band assignments. The Dy^{3+} and Y^{3+} complexes are structurally too similar to differentiate the FTIR spectra of **1** and **4**. From our experience, even if this distinction were possible, the low percentage of Dy^{3+} in the solid solution and the relatively broad nature of the infrared bands would prevent the resolution of specific [Dy(bbppn)Cl] absorptions in the **1[Y]** spectrum.

Table S6. FTIR data for **H_2bbppn** and complexes **1**, **4**, and **1[Y]**

Wavenumber / cm^{-1}		Tentative assignment[13-16]
H_2bbppn	**1**, **4**, **1[Y]** [(a)]	
3600-2600 (s, br)	3410 (w, br) [(b)]	$\nu(O—H)_{phenol,\ methanol}$
3100-2670 (w)	3100-2780 (w)	$\nu(C—H)_{aromatic}$ and $\nu(CH_2, CH_3)$
1600-1420 (s-m)	1600-1410 (s-m)	$\nu(C{=}C, C{=}N)_{aromatic}$ and $\nu(C—N)$
1372 (s)	----	$\delta(O—H)_{phenol}$
1250 (s)	----	$\nu(C—O)_{phenol}$
----	1302 (s)	$\nu(C—O)_{phenolate}$
1200-960 (m-w)	1250-910 (m-w)	$\delta(CH_2, CH_3)$, $\delta(C—H)_{aromatic,\ in\text{-}plane}$

780-720 (s)	800-720 (m)	$\delta(C—H)_{aromatic,\ out\text{-}of\text{-}plane}$
650-420 (w)	660-400 (w)	$\delta(C{=}C)_{aromatic}$ and $\delta(CH_2, CH_3)$

[(a)] The absorption bands for the complexes are the same as their spectra are superimposable (Figure S6).

[(b)] The broad, low intensity band centered at *ca* 3410 cm^{-1} comes from residual methanol employed in the synthesis of the complexes, which was not completely removed even under vacuum.

ν = symmetric and asymmetric stretching; δ = symmetric and asymmetric angular deformation; w = weak; m = medium; s = strong; br = broad.

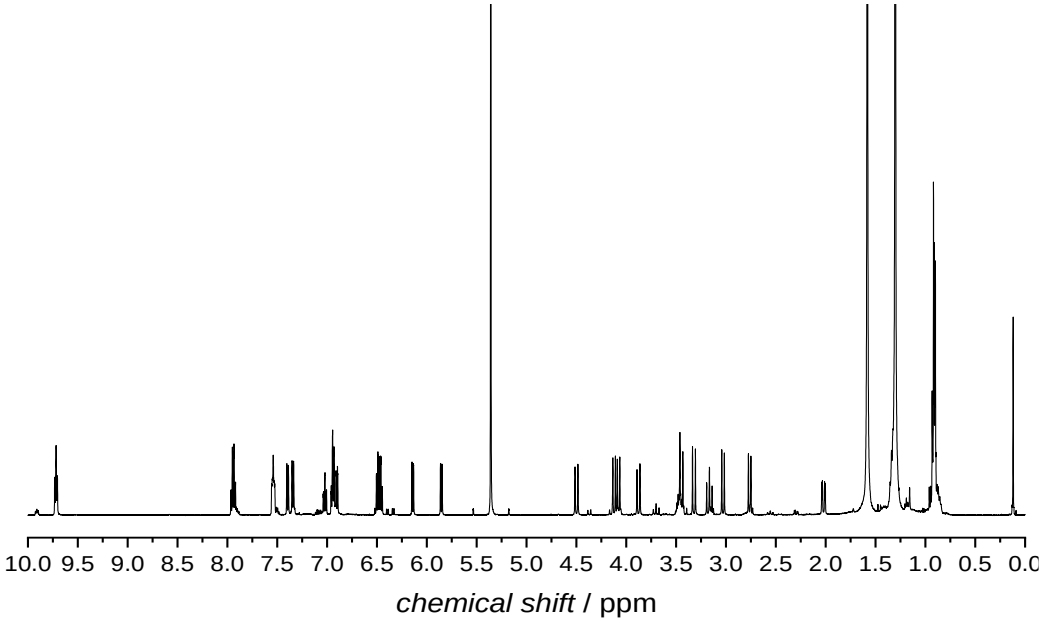

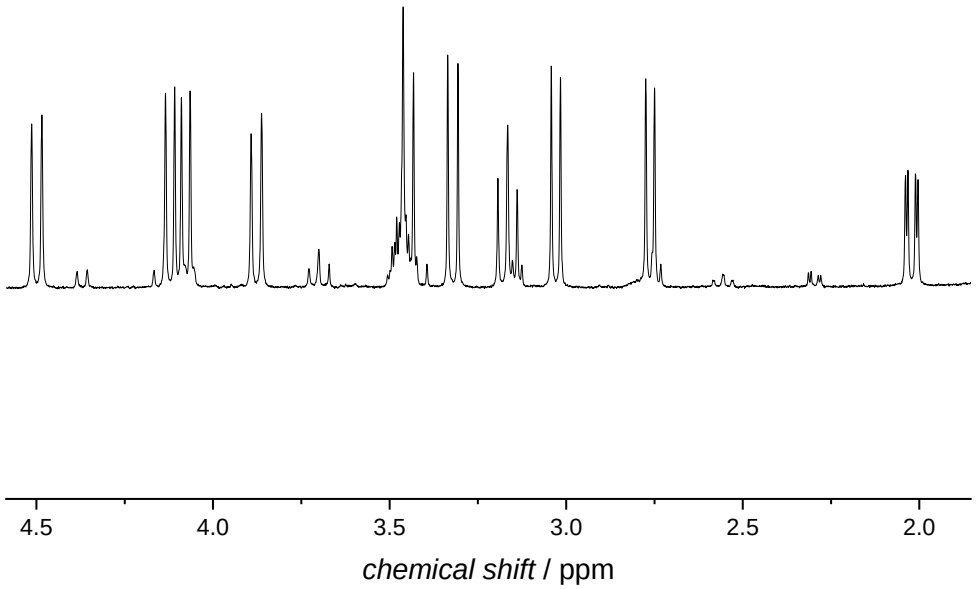

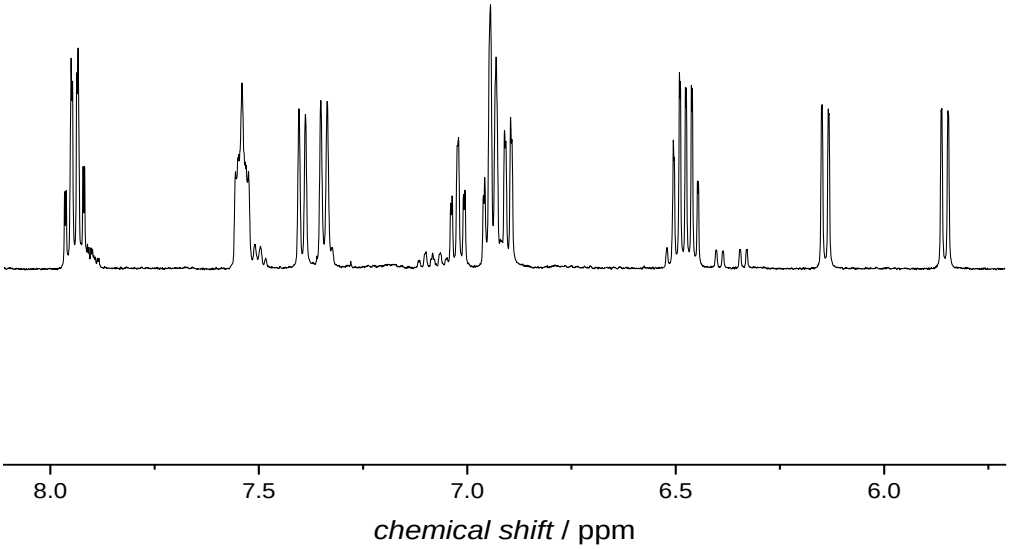

Figure S7. ^{1}H-NMR spectrum for **4** (top) and zooms on two different regions. The spectrum was acquired at 500 MHz ^{1}H Larmor frequency (11.7 T) with a cryogenically cooled probehead in CD_2Cl_2.

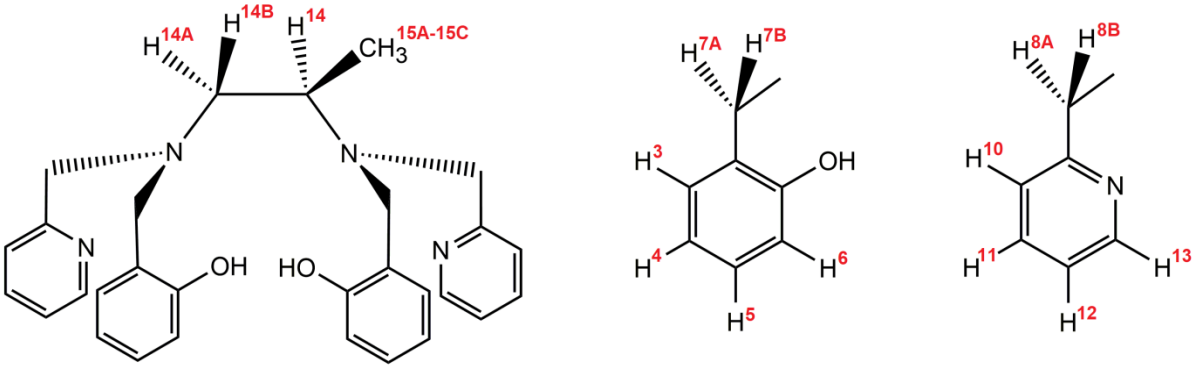

Assignment (*)	Chemical shift, ppm	Multiplicity	Integral
H15A-15C	0.91	m	3
H14A-14B	2.02	dd	1
H8A-8B/8A'-8B'	2.76	d	1
H7A-7B/7A'-7B'	3.03	d	1
H14A-14B	3.17	t	1
H8A-8B/8A'-8B'	3.32	d	1
H7A-7B/7A'-7B'	3.45	d	1
H14	3.48	m	1
H7A-7B/7A'-7B'	3.89	d	1
H8A-8B/8A'-8B'	4.08	d	1
H7A-7B/7A'-7B'	4.12	d	1
H8A-8B/8A'-8B'	4.50	d	1
H4	5.86	d	1
H4	6.14	d	1
H6	6.48	m	2
H5	6.90	d	1
H5	6.938	d	1
H3	6.946	t	1
H3	7.02	t	1
H10	7.34	d	1
H10	7.395	d	1
H11	7.54	m	2
H12	7.94	m	2
H13	9.72	t	2

(*) Based on ^{1}H,^{1}H COSY and ^{1}H,^{13}C HMQC. Data are also in accordance with Yamada *et al.*[17].

Table S7. Tentative peak assignment of the ^{1}H NMR spectrum of **4**. The signal at 5.36 ppm is the residual solvent peak, and the signal at 1.58 ppm is given by trace impurities of water.[18] Signals at 0.84-0.90 ppm (m, CH_3) and 1.27 ppm (b, s, CH_2, Figure S7) are probably due to hydrocarbon-based grease used in distilattion and vacuum apparatus.[19] The peak at 0.12 ppm comes from silicone grease (poly(dimethylsiloxane), s, CH_3).

***Ab initio* calculations**

Table S8. Comparison between the *ab initio* computed electronic structures of the ground $^6H_{15/2}$ multiplet in **1** and **2.** The energy splittings of the whole multiplet and the g-tensor components of the four lowest Kramers doublets are reported

Level	Tong *et al.*[9]	Complex 1
Energy (cm^{-1})		
E_0	0	0
E_1	381	405
E_2	584	705
E_3	655	836
E_4	724	932
E_5	747	949
E_6	759	976
E_7	839	1055
E_0 g-tensor		
g_x	0.00106	0.00209
g_y	0.00137	0.00297
g_z	19.87528	19.94856
E_1 g-tensor		
g_x	0.10691	0.12831
g_y	0.15498	0.15970
g_z	16.92061	16.92131
E_2 g-tensor		
g_x	2.12193	1.65452
g_y	4.82658	2.98470
g_z	11.75264	12.58938
E_3 g-tensor		
g_x	7.69783	1.46270
g_y	6.85361	4.96881
g_z	2.50638	11.95402

Table S9. Angle *γ* between ground KD's easy axis and g_z direction of excited KDs of **1**

Level	Complex 1	
	Energy (cm^{-1})	***γ (°)***
E_0	0	-
E_1	405	0.2
E_2	705	1.1
E_3	836	90.4
E_4	932	102.3
E_5	949	92.9
E_6	976	73.6
E_7	1055	110.2

Table S10. $|m_J\rangle$ composition of the eight lowest Kramers doublets for **1**. The quantization axis is the main magnetic axis of the ground doublet. Only contributions > 20% have been reported.

Level	Complex 1	
	Energy (cm^{-1})	***Composition***
E_0	0	$0.99\|\pm15/2\rangle$
E_1	405	$0.98\|\pm13/2\rangle$
E_2	705	$0.85\|\pm11/2\rangle$
E_3	836	$0.24\|\pm9/2\rangle+$ $0.21\|\pm3/2\rangle+$ $0.29\|\pm1/2\rangle$
E_4	932	$0.26\|\pm9/2\rangle+$ $0.50\|\pm1/2\rangle$
E_5	949	$0.34\|\pm9/2\rangle+$ $0.20\|\pm5/2\rangle+$ $0.22\|\pm3/2\rangle$
E_6	976	$0.24\|\pm7/2\rangle+$ $0.32\|\pm5/2\rangle+$ $0.28\|\pm3/2\rangle$
E_7	1055	$0.47\|\pm5/2\rangle+$ $0.36\|\pm3/2\rangle$

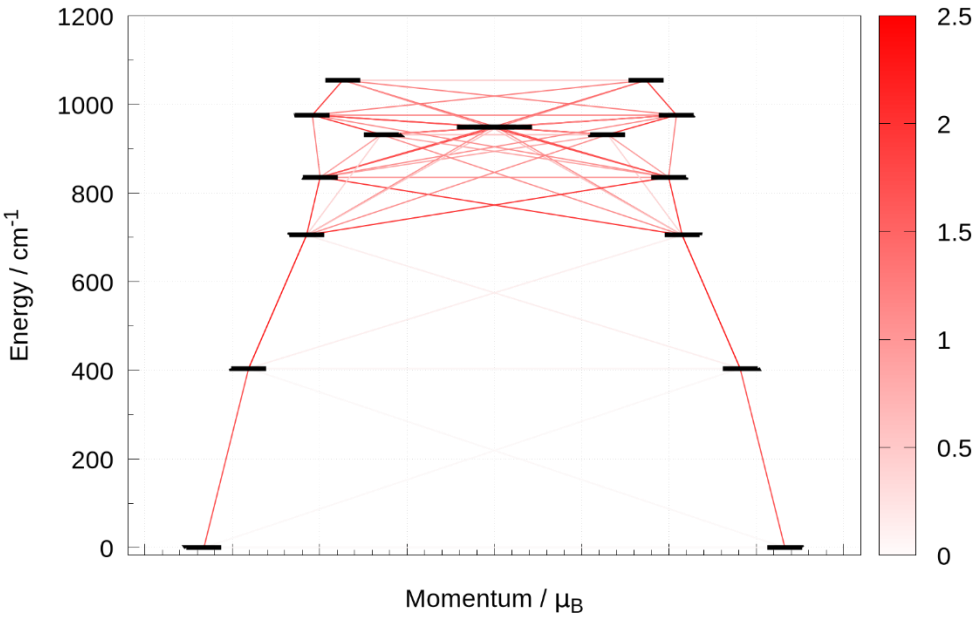

Figure S8. SINGLE_ANISO computed transition magnetic moments among the eight lowest in energy Kramers doublets.

Magnetic Characterization

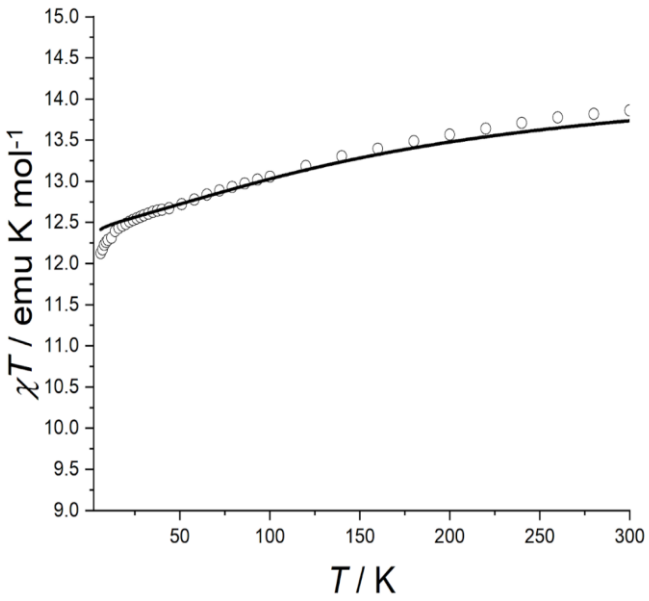

Figure S9. Temperature dependence of the molar magnetic susceptibility multiplied by temperature of a polycrystalline sample of **1** measured with H=1 kOe.
The solid line represents the theoretical value from the *ab initio* computed Crystal Field parameters

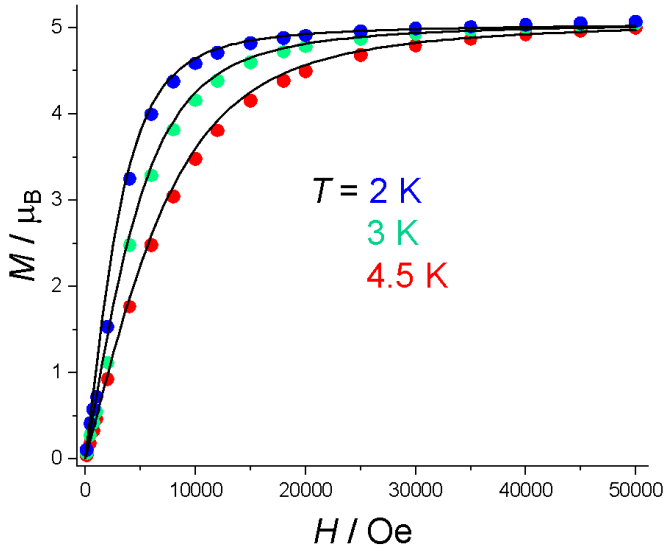

Figure S10. Field dependence of the molar magnetization of **1** at three temperatures.
The solid line represents the theoretical value from the *ab initio* computed Crystal Field parameters.

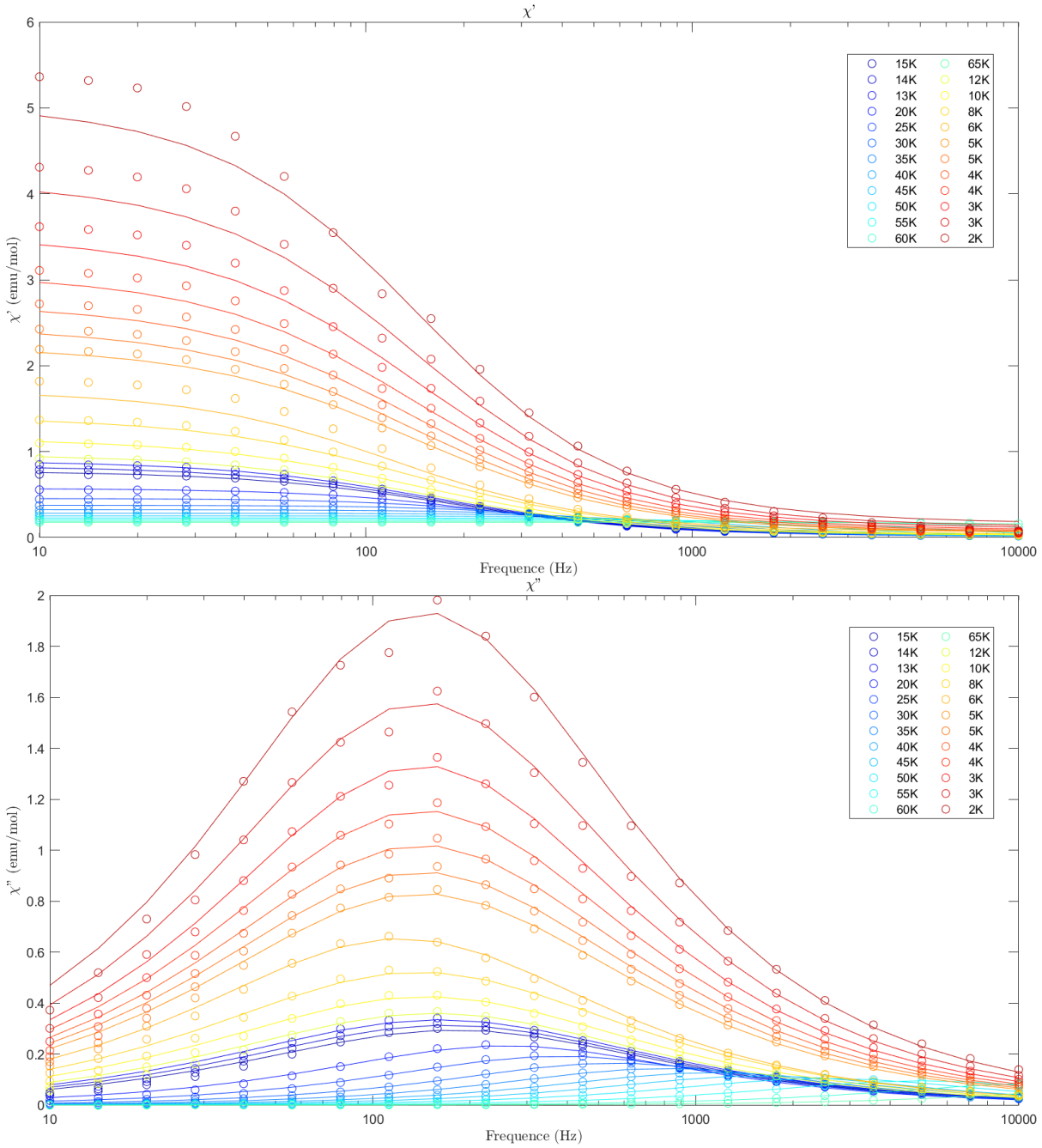

Figure S11. Real (χ ') and imaginary (χ '') ac magnetic susceptibility of **1** recorded at various temperatures and H = 0 Oe. The lines are the fits discussed in the main text.

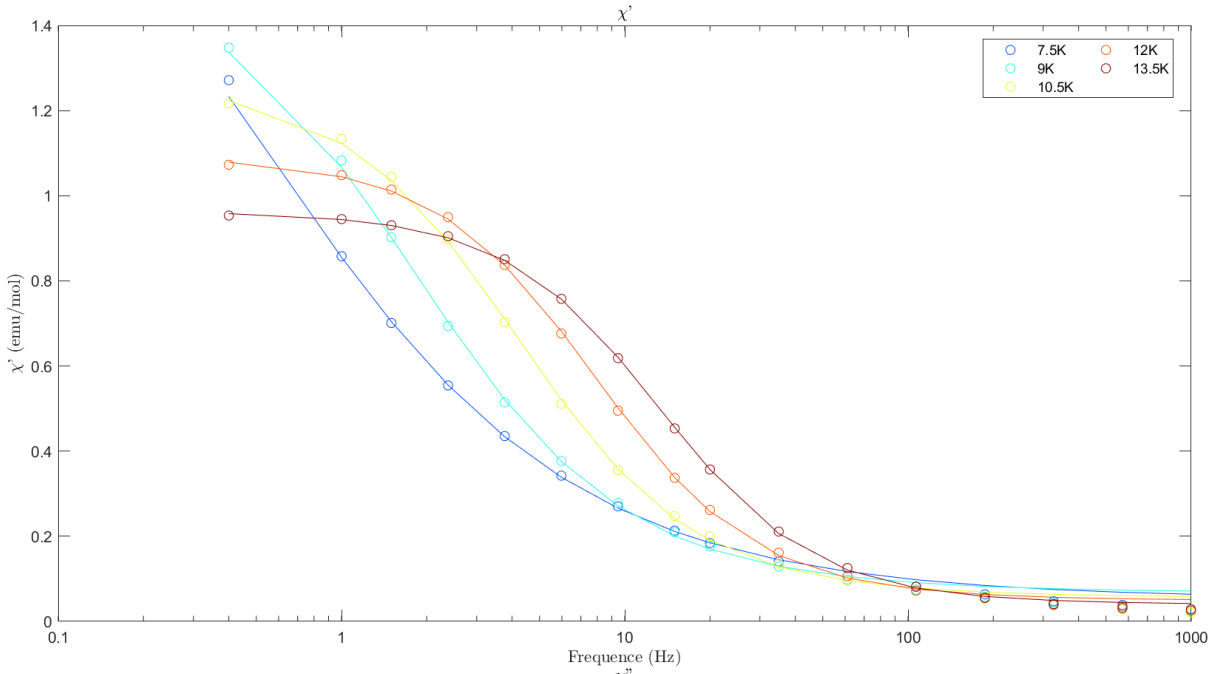
χ'
χ' (emu/mol)
Frequence (Hz)
7.5K
9K
10.5K
12K
13.5K

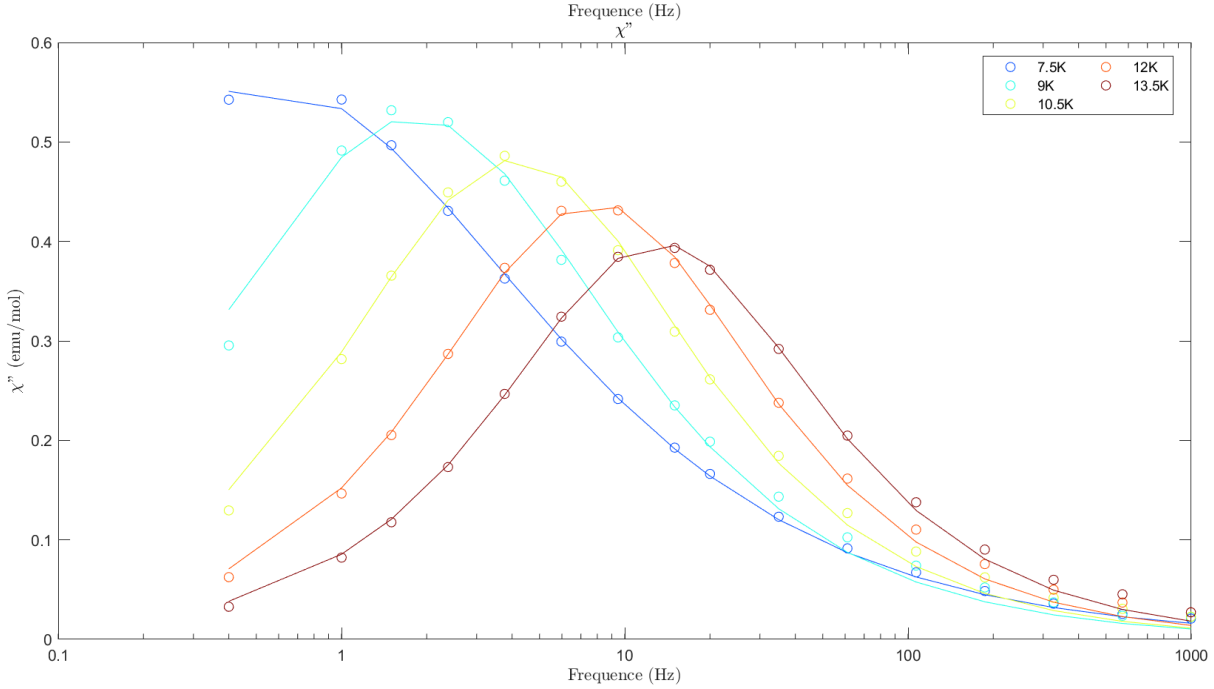
χ"
χ" (emu/mol)
Frequence (Hz)
7.5K
9K
10.5K
12K
13.5K

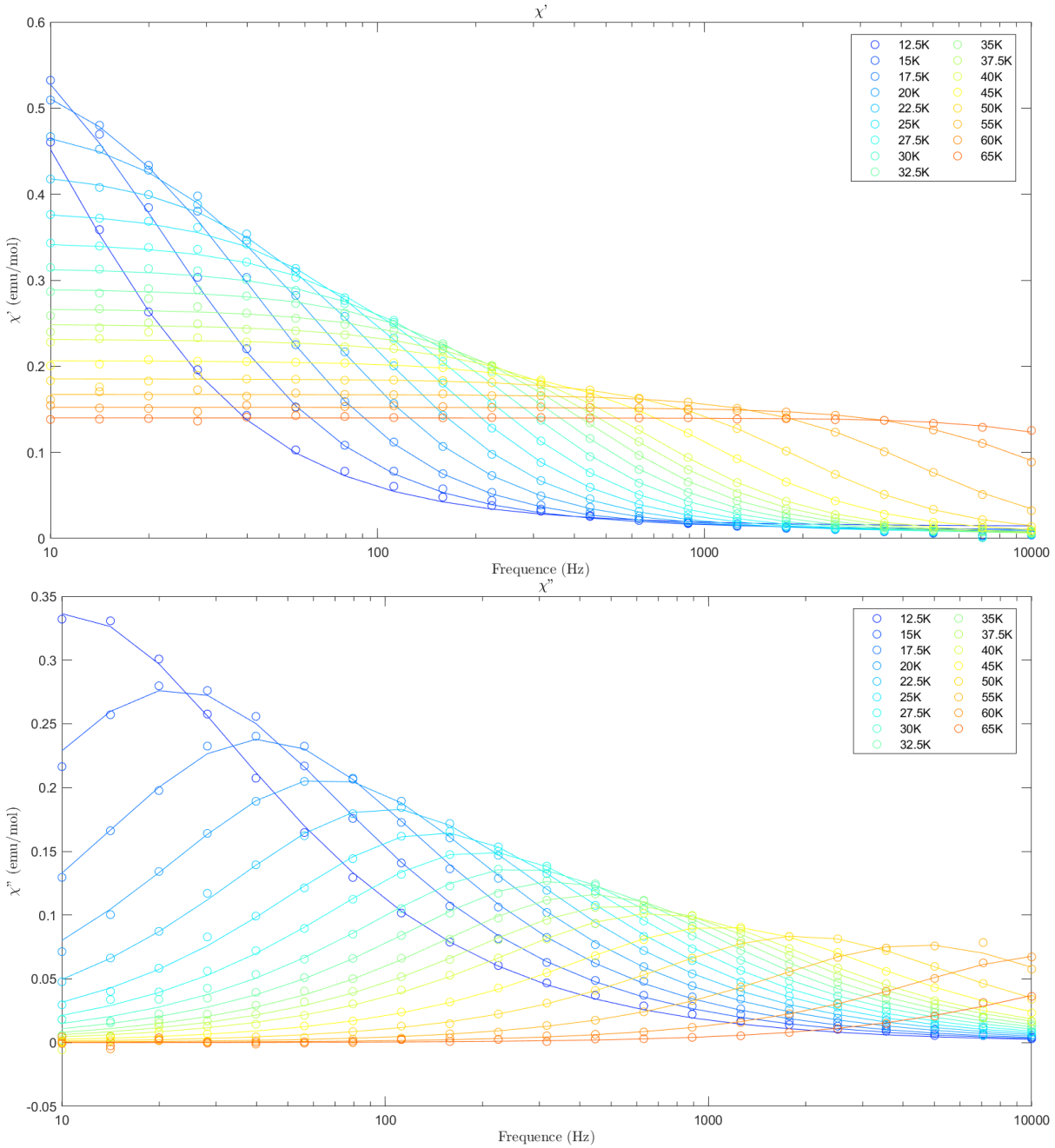

Figure S12. Real (χ ') and imaginary (χ '') ac magnetic susceptibility of **1[Y]** recorded at various temperatures and H = 0 Oe. The lines are the fits discussed in the main text.

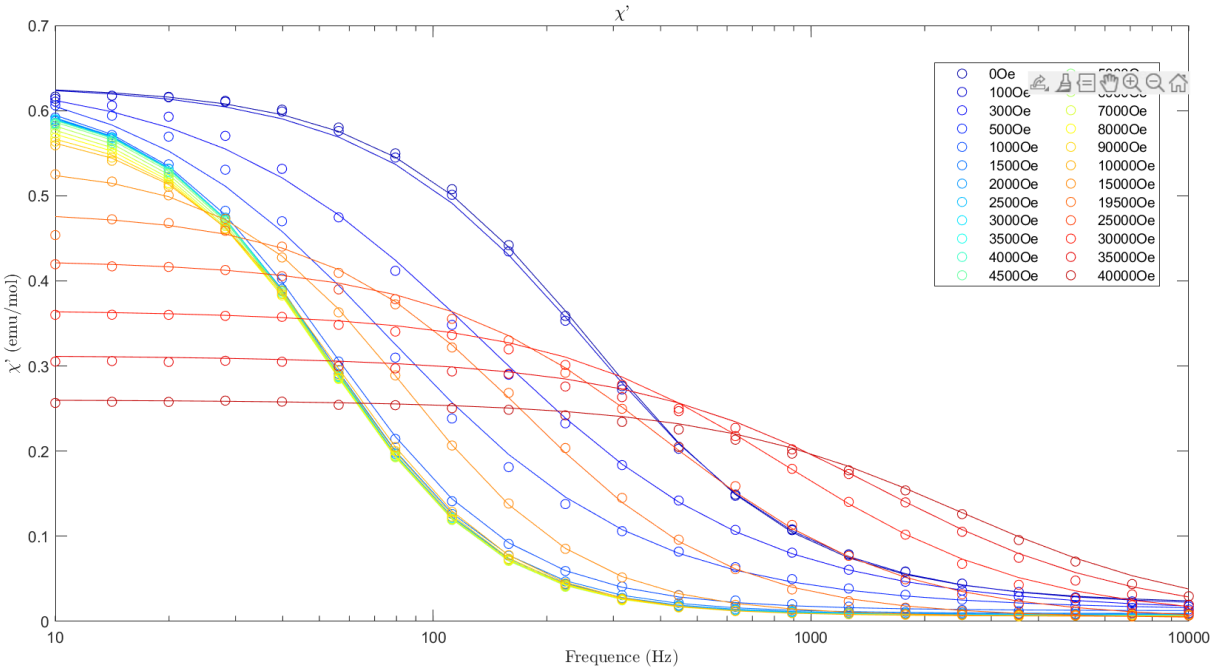
χ'
χ' (emu/mol)
Frequence (Hz)
0Oe
100Oe
300Oe
500Oe
1000Oe
1500Oe
2000Oe
2500Oe
3000Oe
3500Oe
4000Oe
4500Oe
7000Oe
8000Oe
9000Oe
10000Oe
15000Oe
19500Oe
25000Oe
30000Oe
35000Oe
40000Oe

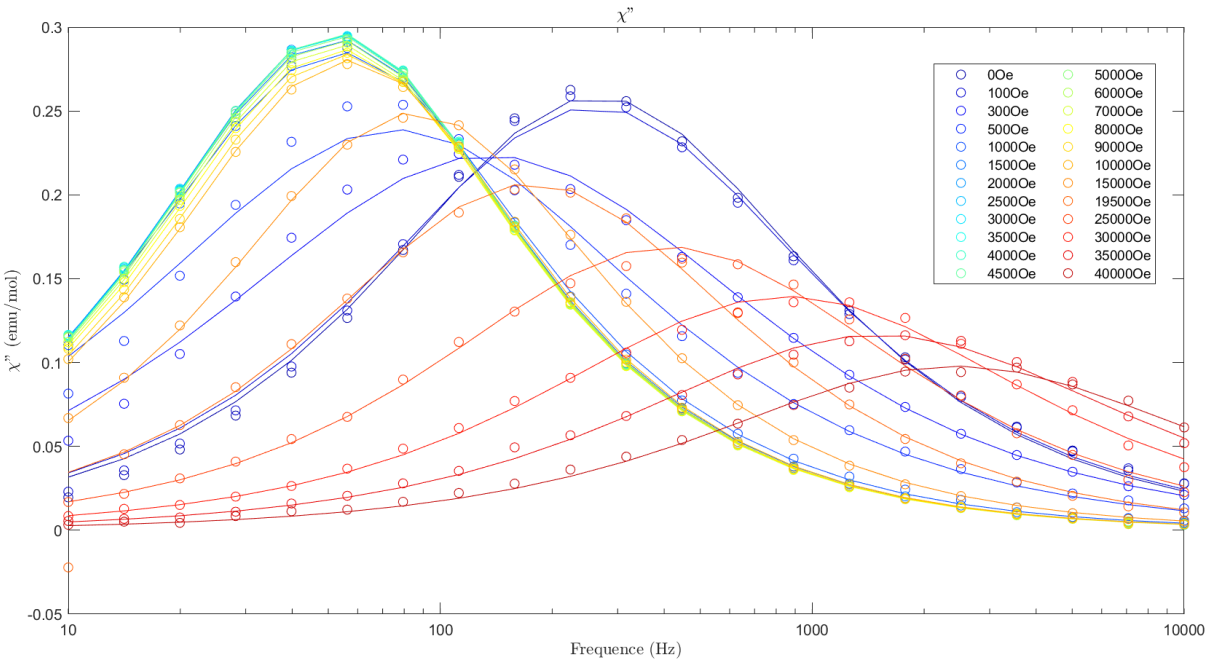
χ"
χ" (emu/mol)
Frequence (Hz)
0Oe
100Oe
300Oe
500Oe
1000Oe
1500Oe
2000Oe
2500Oe
3000Oe
3500Oe
4000Oe
4500Oe
5000Oe
6000Oe
7000Oe
8000Oe
9000Oe
10000Oe
15000Oe
19500Oe
25000Oe
30000Oe
35000Oe
40000Oe

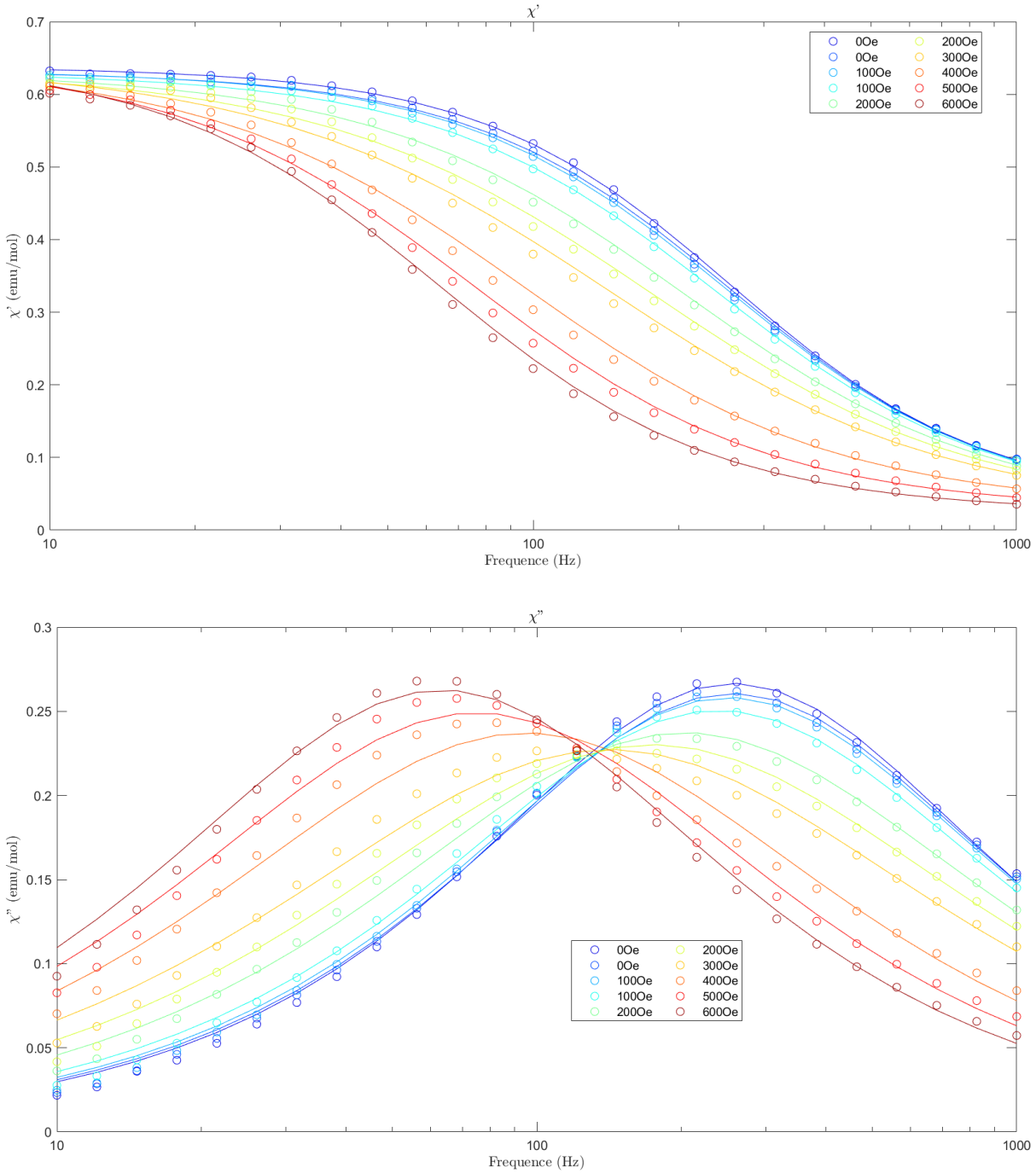

Figure S13. Real (χ ') and imaginary (χ '') ac magnetic susceptibility of **1** recorded at T = 20 K and various magnetic fields. The lines are the fits discussed in the main text.

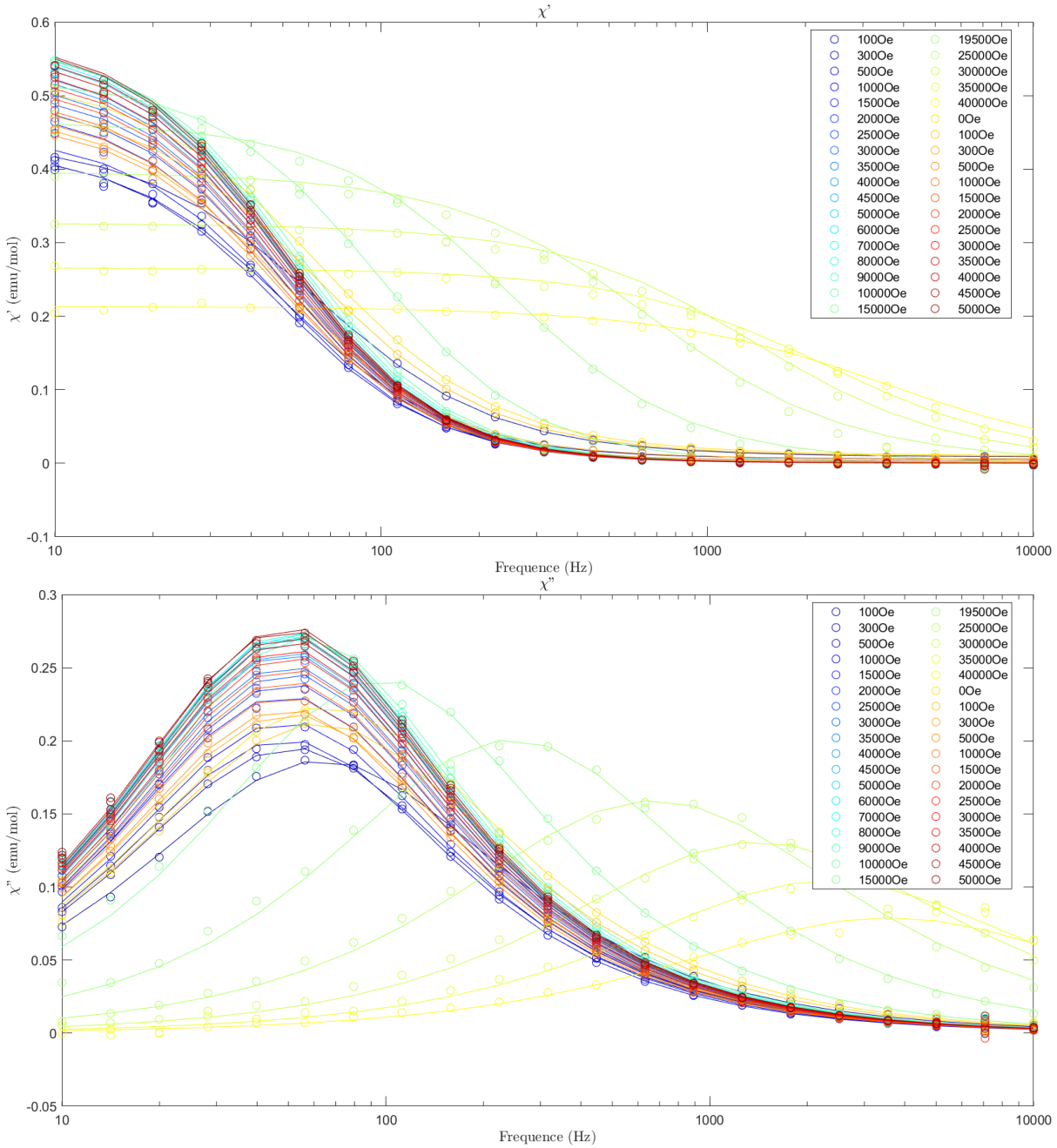

Figure S14. Real (χ ') and imaginary (χ '') ac magnetic susceptibility of **1[Y]** recorded at T = 20 K and various magnetic fields. The lines are the fits discussed in the main text.

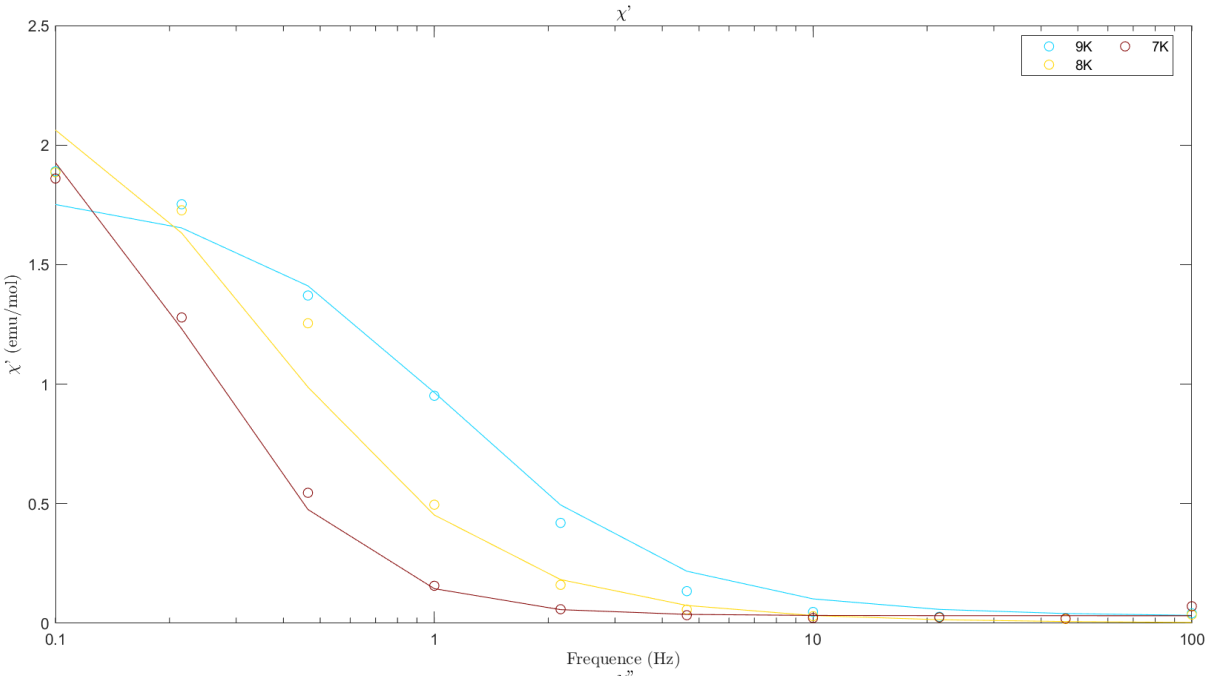
χ'
9K
7K
8K
χ' (emu/mol)
Frequence (Hz)

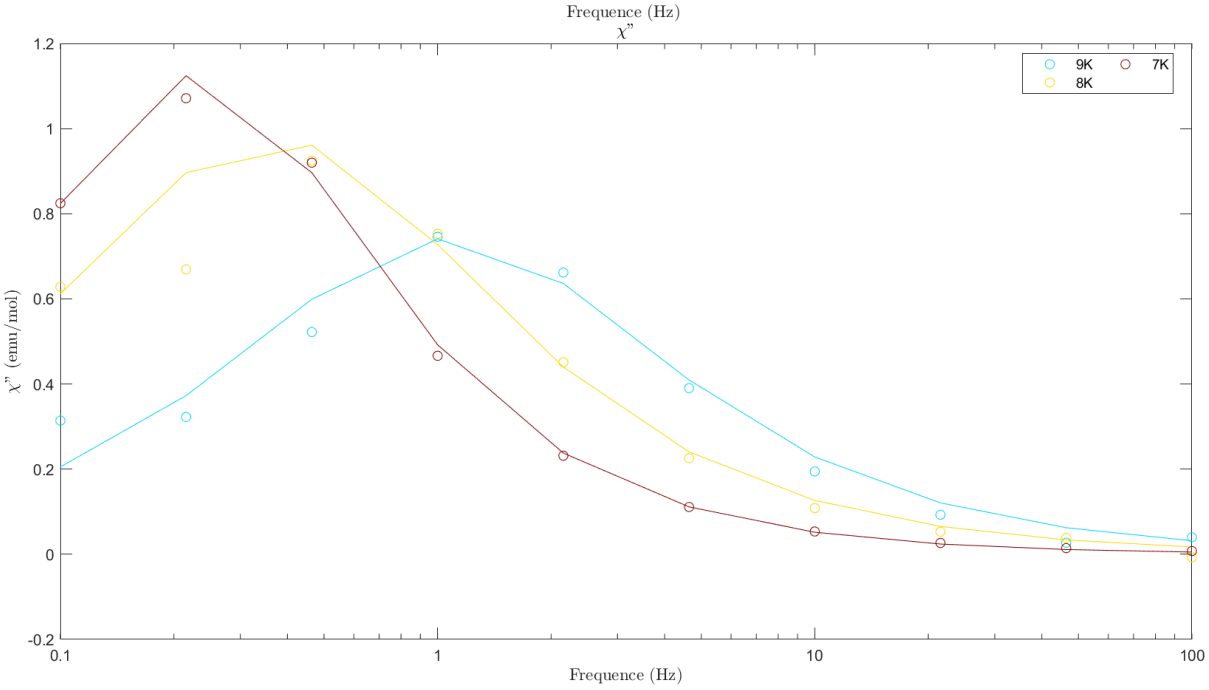
χ"
9K
7K
8K
χ" (emu/mol)
Frequence (Hz)

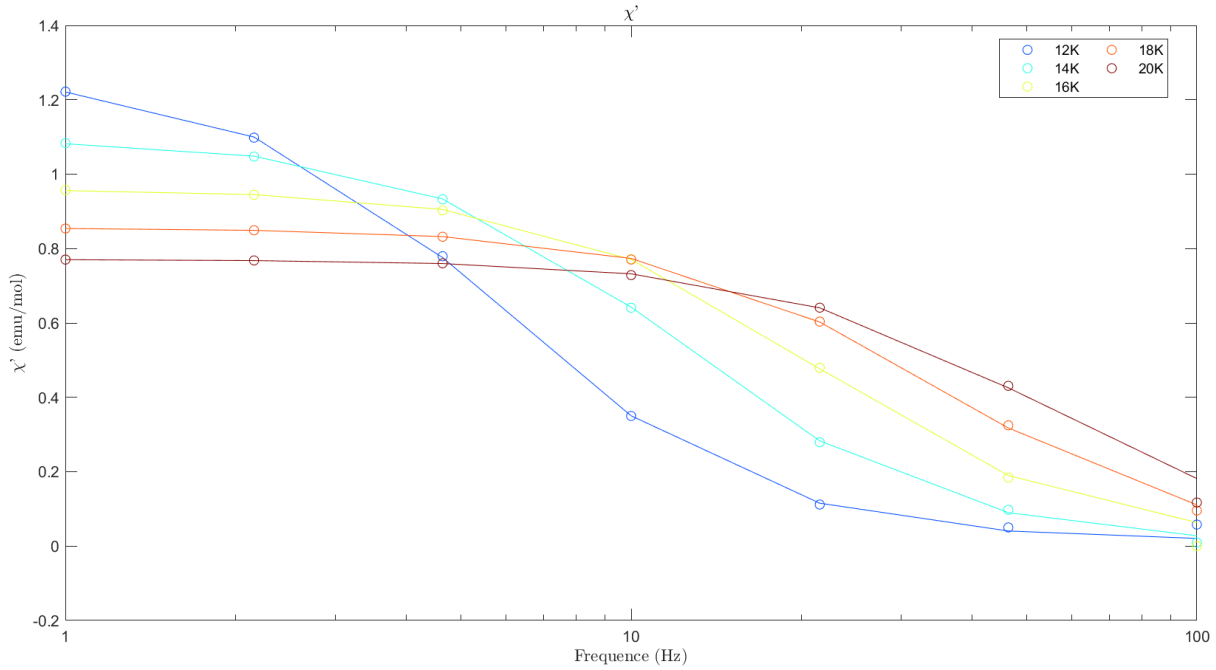
χ'
12K
14K
16K
18K
20K
χ' (emu/mol)
Frequence (Hz)

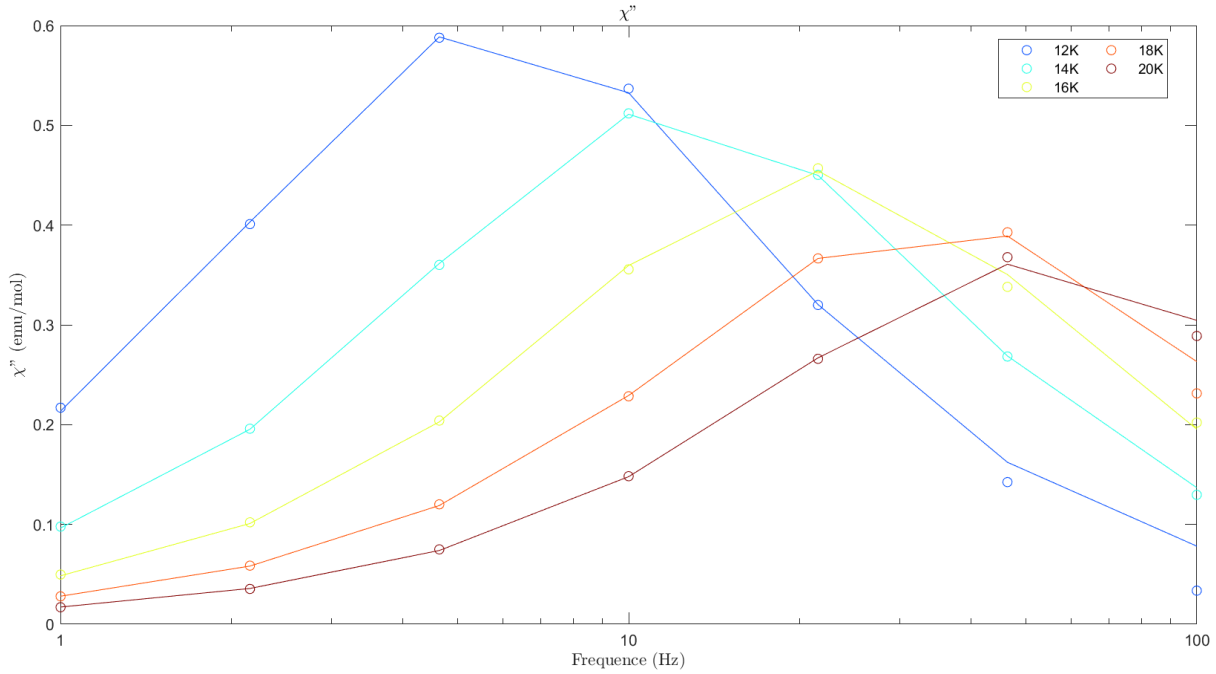
χ"
12K
14K
16K
18K
20K
χ" (emu/mol)
Frequence (Hz)

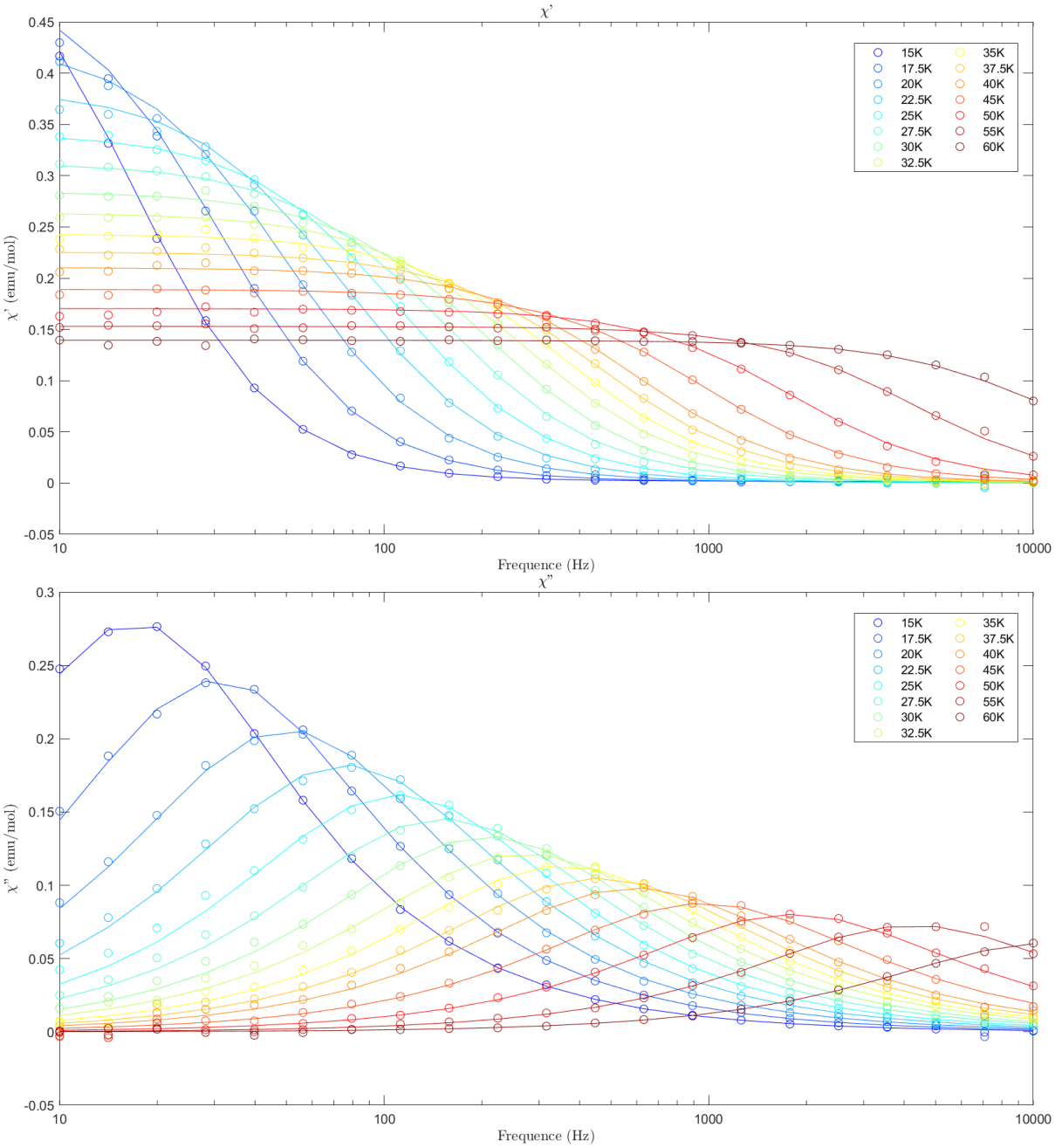

Figure S15. Real (χ ') and imaginary (χ '') ac magnetic susceptibility of **1** recorded at various temperatures and H = 1.6 kOe. The lines are the fits discussed in the main text.

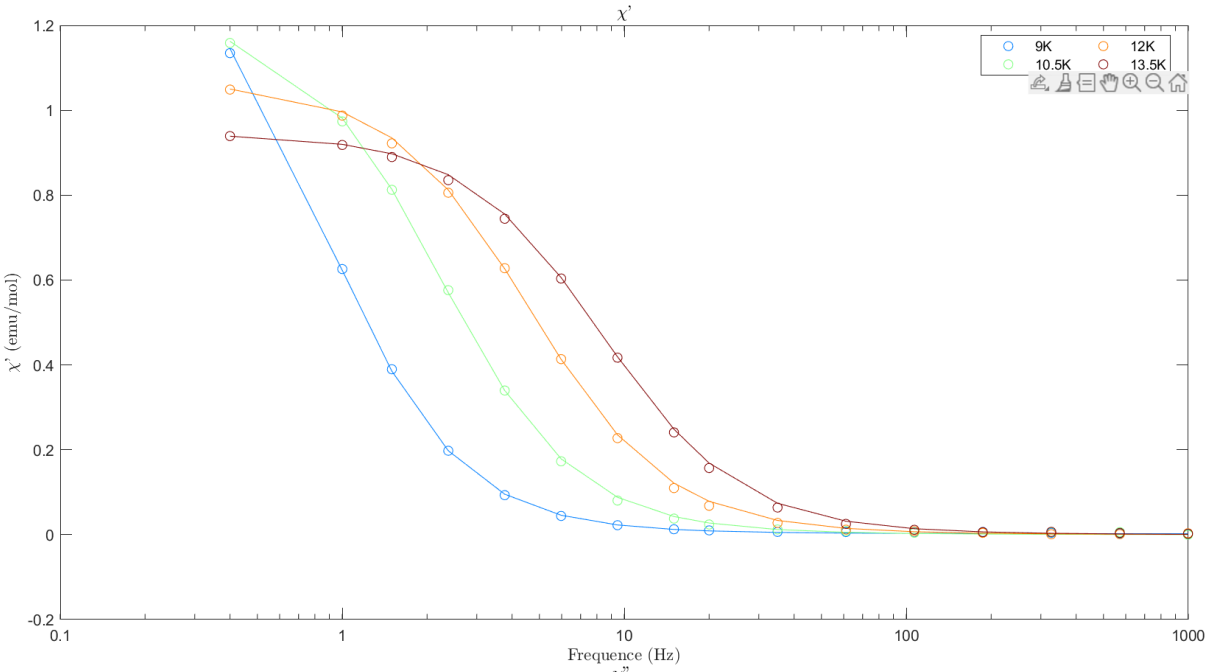
χ'
9K
10.5K
12K
13.5K
χ' (emu/mol)
Frequence (Hz)

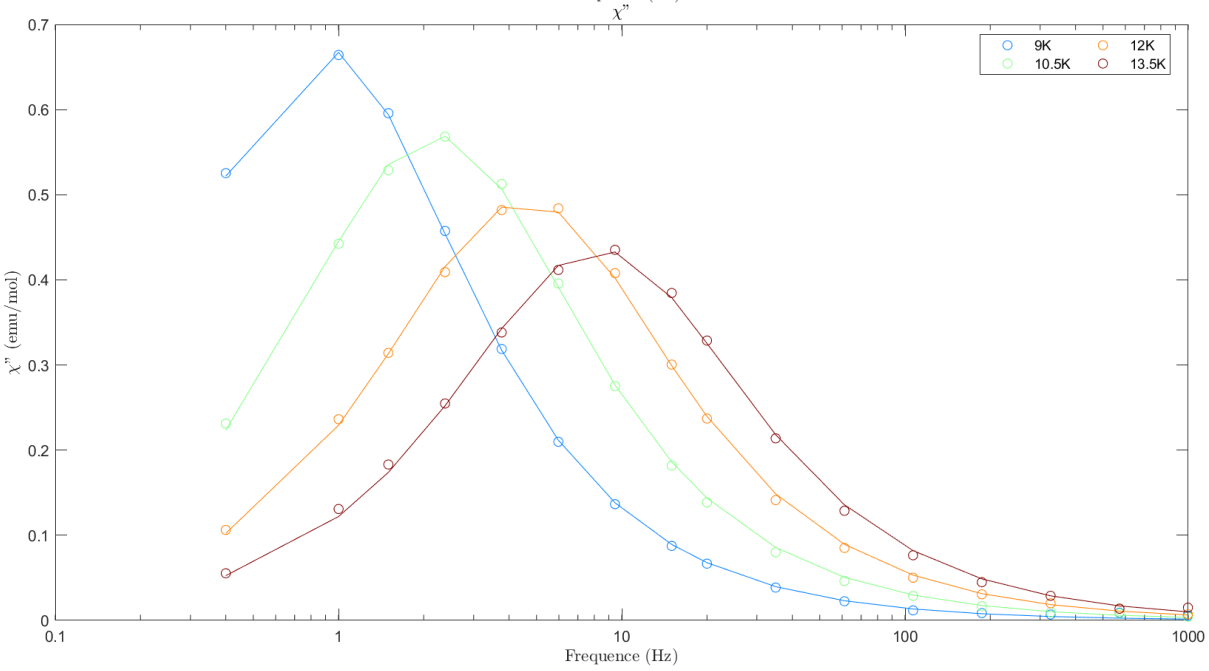
χ"
9K
10.5K
12K
13.5K
χ" (emu/mol)
Frequence (Hz)

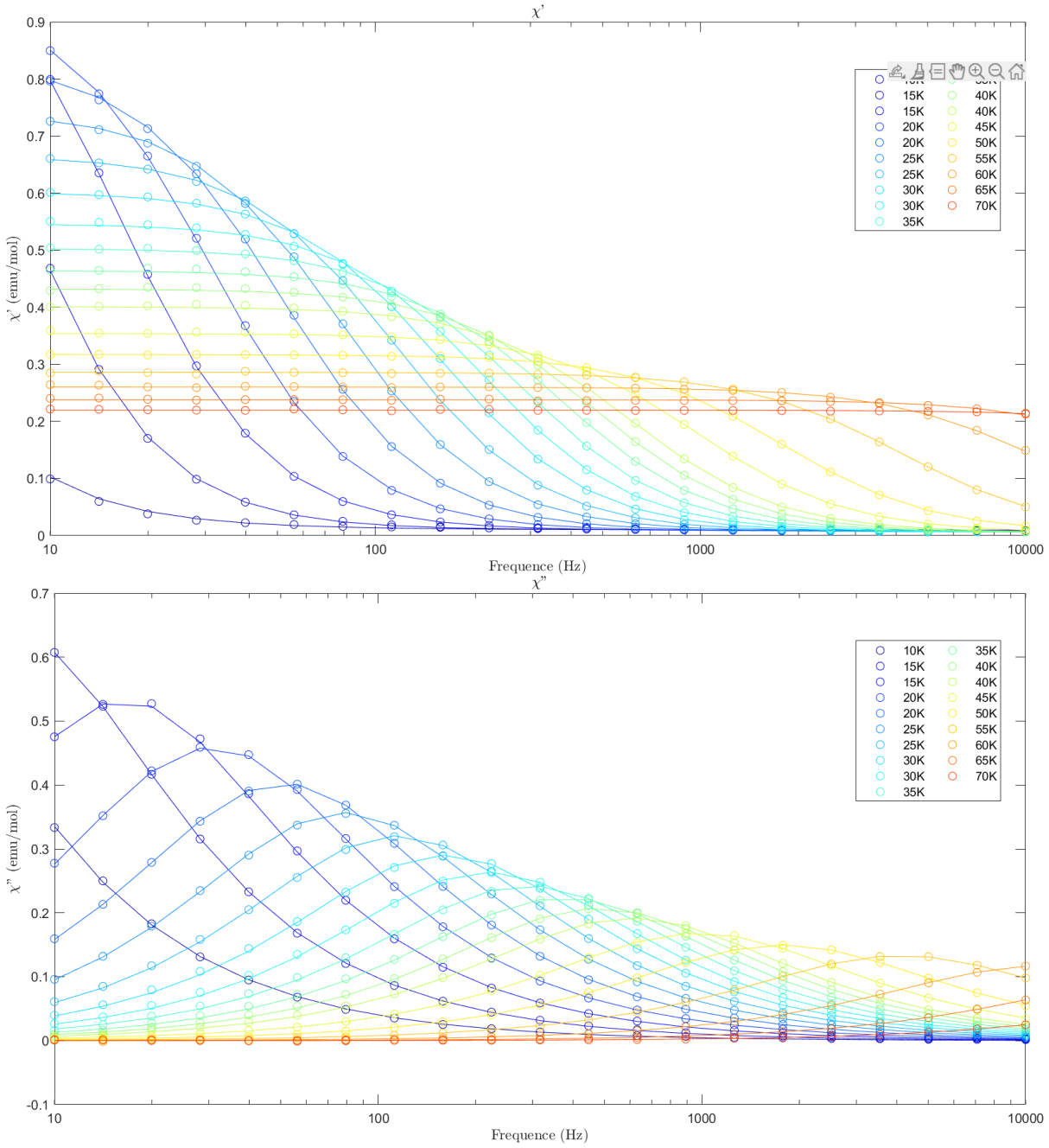

Figure S16. Real (χ ') and imaginary (χ '') ac magnetic susceptibility of **1** recorded at various temperatures and H = 1.6 kOe. The lines are the fits discussed in the main text.

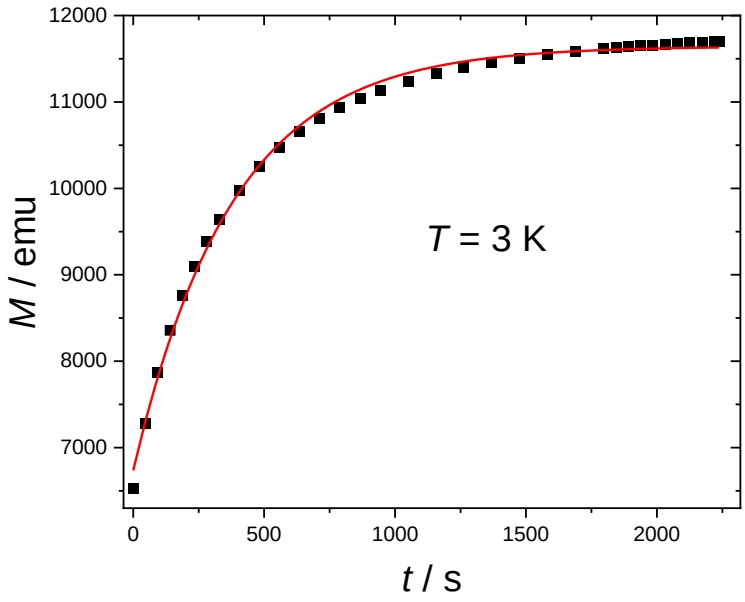

Figure S17. Fit of the decay of the magnetization at *T* = 3 K for **1**.

Table S11. Fitting results of the decay of the magnetization.

Temperature / K	**Relaxation time / s**
1.85	423(10)
1.9	379(9)
2	369(10)
2.1	350(10)
2.2	320(8)
2.3	310(8)
2.5	255(6)
2.7	231(6)
2.9	203(4)
3.1	184(3)
3.4	122(2)
3.7	83(1)
4	52(2)

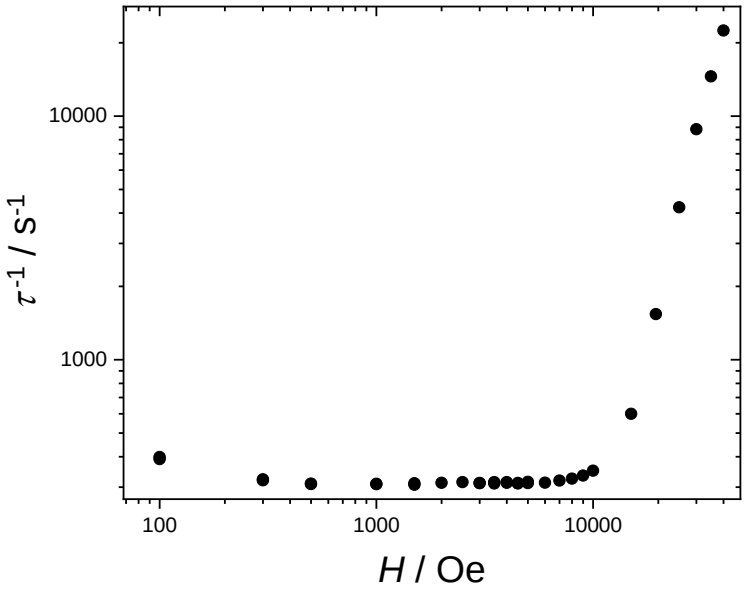

Figure S18. Field dependence of the relaxation rate for **1[Y]** measured at 20 K.

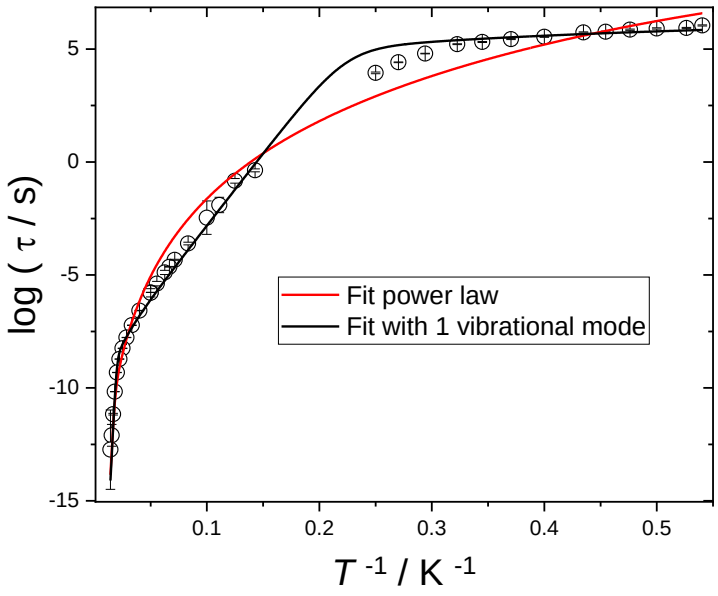

Figure S19. Alternative fits of the relaxation time of **1** at H = 1.6 kOe. Red line: using a CT^n expression for the Raman term. Best fit: n = 5.0(1), C = 4(2) 10^{-5}, D = 1(6) 10^{-4}. Black line: using a single vibrational mode. Best fit: ω_1 = 64(2) K, B = 10.0(6) 10^3, D = 1.5(2) 10^{-3}. Orbach parameters were kept fixed at the values reported in the main text.

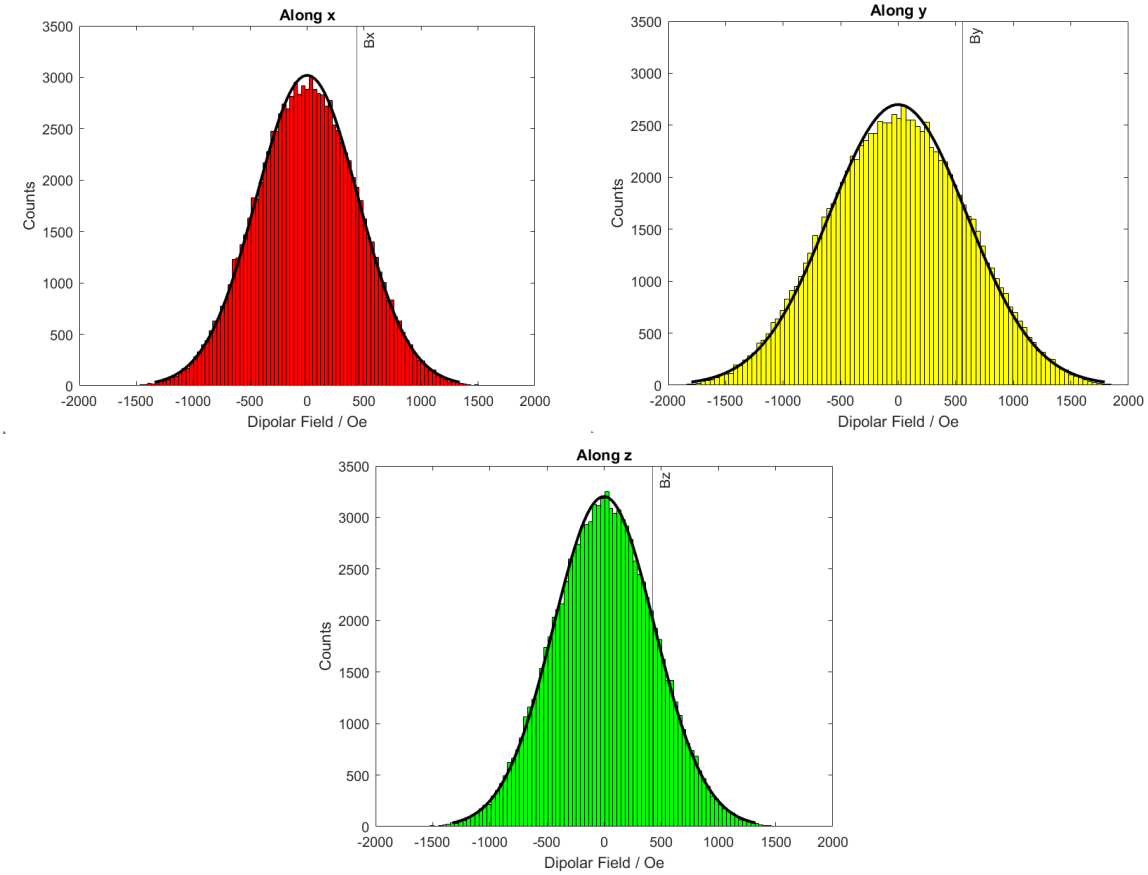

Figure S20. Distribution of dipolar fields in zero external magnetic field inside a crystal. The distribution was calculated with 10^5 random spin configurations (all with zero net magnetization) in a crystal composed by a central cell surrounded by 5 cubic shells of crystallographic cells. The directions x, y and z are the principal magnetic axes. The mean of the absolute value of the magnetic field along each direction is marked as a vertical line in the plots.

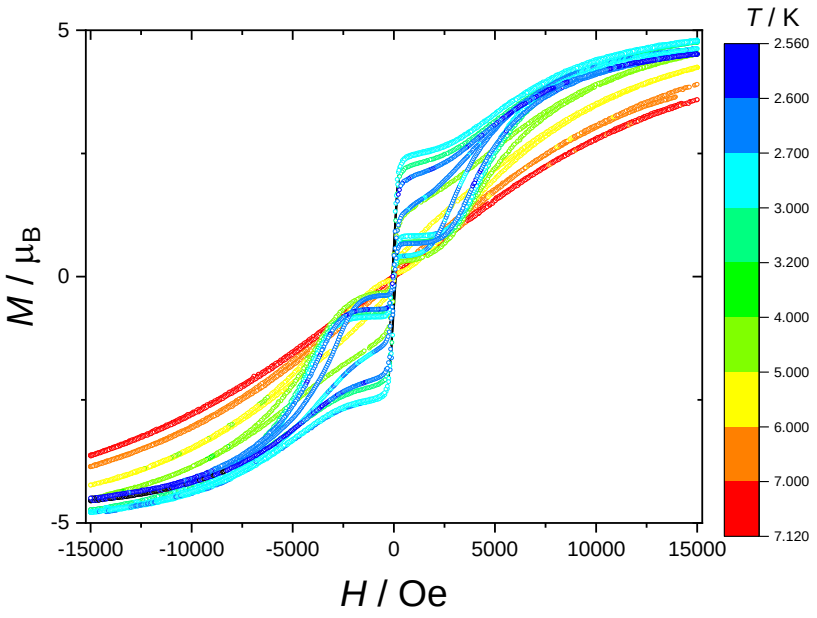

Figure S21. Temperature (top) and field sweep rate (bottom) dependence of the hysteresis loops of **1[Y]**.

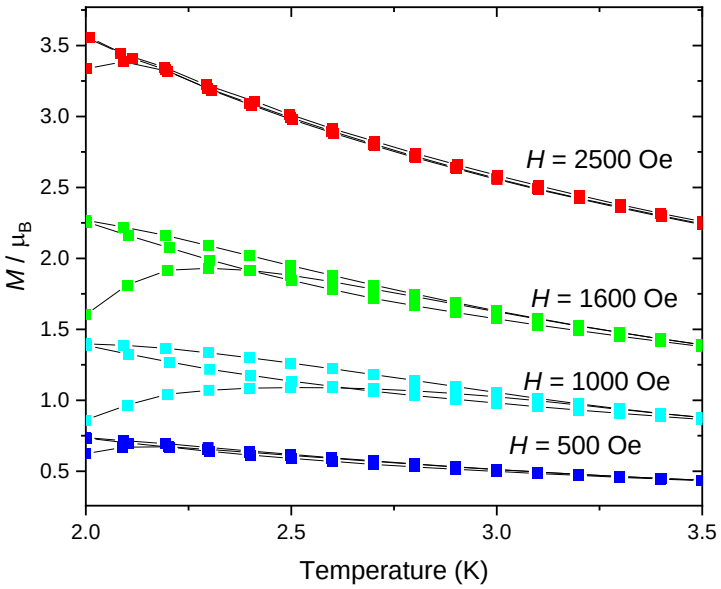

Figure S22. ZFC-FC curves recorded for **1** at different applied magnetic fields.

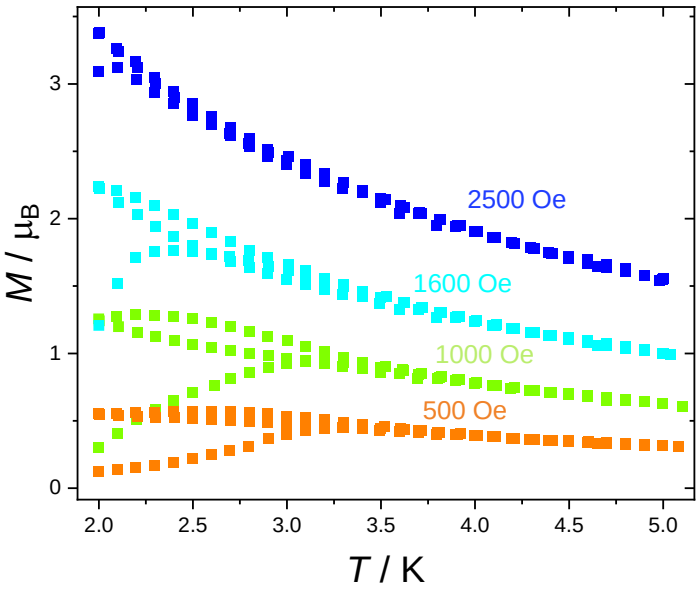

Figure S23. ZFC-FC curves recorded for **1[Y]** at different applied magnetic fields.

NMR characterization

The magnetic susceptibility of DOTA in solution

The calculated magnetic susceptibility of DyDOTA in solution was obtained by averaging the susceptibility of the lowest energy water configuration over four positions 90° away from each other. These orientations were obtained by rotating around the Dy-O_{water} bond so as to achieve the symmetrization of the tensor that can be expected in a fluid water solution. The susceptibility calculated in this way is roughly 10% higher than the one that reproduces the experimental data[20] following the procedure described in literature.[21] This is in line with the intrinsic overestimation of the ionic character of bonding intrinsic in the CASSCF-PT2-level calculations and may also reflect crystal packing effects.

Simulation of the NMR spectra

The calculated relaxation rates, not including the contact relaxation and the effect of chemical exchange are reflected in the linewidths and in the intensity of the signals. The linewidth and intensity of each single resonance is given by the discrete fourier transform of the signal in the time domain:

$$S(t) = I \exp\left[(\mathrm{i}2\pi\delta\mathrm{B}_0 - \mathrm{R}_2)\mathrm{t}_{\mathrm{aq}}\right]$$

Where:

$$\mathrm{t}_{\mathrm{aq}} = t_{DE} + 2\,kt_{dw}, k = 1{,}65536$$

$$I = sin\theta\left(\sin^2\alpha + \sqrt{\cos\theta\,(1-\cos\alpha)^2}\right)(1-\exp(-R_1 t_{rec}))\exp(-R_2 t_{DE})$$

$t_{rec} = t_{aq,max} + 3\cdot 10^{-5} + d_1;\quad \theta = \arctan\left(\frac{\omega_{nut}}{|2\pi\delta B_0|}\right);\quad \alpha = \frac{\pi}{2}\frac{t_p}{t_{90}}\sqrt{\omega_{nut}^2 + (2\pi\delta B_0)^2};\quad t_p = 2\cdot 10^{-7}\,s; t_{90} = 4.5\cdot 10^{-6}\,s; \omega_{nut} = \frac{1}{4\cdot t_{90}}; d_1 = 1\cdot 10^{-5}\,s; t_{dw} = 4\cdot 10^{-7}\,s$

References

1. D. D. Perrin and W. L. Armarego, *Purification of Laboratory Chemicals*, Butterworth-Heinemann, Oxford, 3rd edn., 1997.
2. A. Neves, S. M. D. Erthal, I. Vencato, A. S. Ceccato, Y. P. Mascarenhas, O. R. Nascimento, M. Horner and A. A. Batista, *Inorganic Chemistry*, 1992, **31**, 4749-4755.
3. Y. Yamada, S.-I. Takenouchi, Y. Miyoshi and K.-I. Okamoto, *Journal of Coordination Chemistry*, 2010, **63**, 996-1012.
4. T. Gregório, J. d. M. Leão, G. A. Barbosa, J. d. L. Ramos, S. Om Kumar Giese, M. Briganti, P. C. Rodrigues, E. L. de Sá, E. R. Viana, D. L. Hughes, L. D. Carlos, R. A. S. Ferreira, A. G. Macedo, G. G. Nunes and J. F. Soares, *Inorganic Chemistry*, 2019, **58**, 12099-12111.
5. C. F. Macrae, I. Sovago, S. J. Cottrell, P. T. Galek, P. McCabe, E. Pidcock, M. Platings, G. P. Shields, J. S. Stevens and M. Towler, *J. Appl. Crystallogr.*, 2020, **53**, 226-235.
6. G. Sheldrick, *Acta Crystallographica, Section A: Foundations and Advances*, 2008, **64**, 112-122.
7. G. M. Sheldrick, *Acta Crystallographica Section A*, 2015, **71**, 3-8.
8. L. J. Farrugia, *Journal of Applied Crystallography*, 2012, **45**, 849-854.
9. K. Brandenburg, *Journal*, 2006.
10. J. Liu, Y.-C. Chen, J.-L. Liu, V. Vieru, L. Ungur, J.-H. Jia, L. F. Chibotaru, Y. Lan, W. Wernsdorfer, S. Gao, X.-M. Chen and M.-L. Tong, *J. Am. Chem. Soc.*, 2016, **138**, 5441-5450.
11. Z. Jiang, L. Sun, Q. Yang, B. Yin, H. Ke, J. Han, Q. Wei, G. Xie and S. Chen, *J. Mater. Chem. C*, 2018, **6**, 4273-4280.
12. M. Llunell, D. Casanova, J. Cirera, P. Alemany and S. Alvarez.
13. G. Świderski, M. Kalinowska, J. Malejko and W. Lewandowski, *Vibrational Spectroscopy*, 2016, **87**, 81-87.
14. D. L. Pavia, G. M. Lampman, G. S. Kriz and J. A. Vyvyan, *Introduction to spectroscopy*, Cengage Learning, Stamford (CT), 5th edn., 2014.
15. K. Nakamoto, *Infrared and Raman Spectra of Inorganic and Coordination Compounds*, Wiley-Interscience, New York, 5th edn., 1997.
16. N. B. Colthup, L. H. Daly and S. E. Wiberley, *Introduction to Infrared and Raman Spectroscopy*, Academic Press, 3rd edn., 1990.
17. Y. Yamada, S.-I. Takenouchi, Y. Miyoshi and K.-I. Okamoto, *J. Coord. Chem.*, 2010, **63**, 996-1012.
18. H. E. Gottlieb, V. Kotlyar and A. Nudelman, *J. Org. Chem.*, 1997, **62**, 7512-7515.
19. G. R. Fulmer, A. J. Miller, N. H. Sherden, H. E. Gottlieb, A. Nudelman, B. M. Stoltz, J. E. Bercaw and K. I. Goldberg, *Organometallics*, 2010, **29**, 2176-2179.
20. M. P. M. Marques, C. F. G. C. Geraldes, A. D. Sherry, A. E. Merbach, H. Powell, D. Pubanz, S. Aime and M. Botta, *Journal of Alloys and Compounds*, 1995, **225**, 303-307.
21. S. Aime, M. Botta and G. Ermondi, *Inorganic Chemistry*, 1992, **31**, 4291-4299.